

See discussions, stats, and author profiles for this publication at: <https://www.researchgate.net/publication/325182536>

Dredging and canal gate technologies in Portus, the ancient harbour of Rome, reconstructed from event stratigraphy and multi-proxy sediment analysis

Article in *Quaternary International* · May 2018

DOI: 10.1016/j.quaint.2018.05.018

CITATIONS

0

READS

99

11 authors, including:



Agathe Lisé-Pronovost

La Trobe University

25 PUBLICATIONS **197** CITATIONS

[SEE PROFILE](#)



Jean-Philippe Goiran

French National Centre for Scientific Research

114 PUBLICATIONS **735** CITATIONS

[SEE PROFILE](#)



Guillaume St-Onge

Université du Québec à Rimouski UQAR

167 PUBLICATIONS **1,898** CITATIONS

[SEE PROFILE](#)



Andy I R Herries

La Trobe University

90 PUBLICATIONS **2,371** CITATIONS

[SEE PROFILE](#)

Some of the authors of this publication are also working on these related projects:



Arctic change [View project](#)



Forum on Nuclear Cooperation In Asia (FNCA) [View project](#)

Accepted Manuscript

Dredging and canal gate technologies in Portus, the ancient harbour of Rome, reconstructed from event stratigraphy and multi-proxy sediment analysis

A. Lisé-Pronovost, F. Salomon, J.-P. Goiran, G. St-Onge, A.I.R. Herries, J.-C. Montero-Serrano, D. Heslop, A.P. Roberts, V. Levchenko, A. Zawadzki, H. Heijnis



PII: S1040-6182(17)31397-6

DOI: [10.1016/j.quaint.2018.05.018](https://doi.org/10.1016/j.quaint.2018.05.018)

Reference: JQI 7428

To appear in: *Quaternary International*

Received Date: 2 November 2017

Revised Date: 27 April 2018

Accepted Date: 11 May 2018

Please cite this article as: Lisé-Pronovost, A., Salomon, F., Goiran, J.-P., St-Onge, G., Herries, A.I.R., Montero-Serrano, J.-C., Heslop, D., Roberts, A.P., Levchenko, V., Zawadzki, A., Heijnis, H., Dredging and canal gate technologies in Portus, the ancient harbour of Rome, reconstructed from event stratigraphy and multi-proxy sediment analysis, *Quaternary International* (2018), doi: 10.1016/j.quaint.2018.05.018.

This is a PDF file of an unedited manuscript that has been accepted for publication. As a service to our customers we are providing this early version of the manuscript. The manuscript will undergo copyediting, typesetting, and review of the resulting proof before it is published in its final form. Please note that during the production process errors may be discovered which could affect the content, and all legal disclaimers that apply to the journal pertain.

Dredging and Canal Gate Technologies in Portus, the Ancient Harbour of Rome, Reconstructed from Event Stratigraphy and Multi-Proxy Sediment Analysis

Lisé-Pronovost, A.¹, Salomon, F.^{2,3}, Goiran, J.-P.⁴, St-Onge, G.⁵, Herries, A. I. R.¹, Montero-Serrano, J.-C.⁵, Heslop, D.⁶, Roberts, A. P.⁶, Levchenko, V.⁷, Zawadzki, A.⁷, Heijnis, H.⁷

¹The Australian Archaeomagnetism Laboratory, Palaeoscience Labs, Department of Archaeology and History, La Trobe University, Melbourne Campus, Bundoora, 3086, VIC, Australia

²Laboratoire Image Ville Environnement UMR 7362, Université de Strasbourg, 3 rue de l'Argonne 67083 Strasbourg cedex, France

³Department of Archaeology, University of Southampton, Southampton SO17 1BF, United Kingdom

⁴Centre national de la recherche scientifique, Maison de l'Orient et de la Méditerranée, Lyon 69365, France

⁵Institut des sciences de la mer de Rimouski, Canada Research Chair in Marine Geology, Université du Québec à Rimouski and GEOTOP, Rimouski G5L 2Z9, Québec, Canada

⁶Research School of Earth Sciences, Australian National University, Canberra, 2601, ACT, Australia

⁷Australian Nuclear Science and Technology Organisation (ANSTO), Lucas Heights, 2234, NSW, Australia

ABSTRACT

Ancient harbours are rich archives of human-environment interaction. However, dating harbour deposits and correlating their stratigraphy is a major challenge because of typically high sedimentation rates over short periods and possible curative dredging events. Portus, the maritime harbour of Rome at the height of the Roman Empire, was a port complex composed of basins and canals connecting the commercial harbour to Rome via the Tiber River. Sediment core CPS1 in the narrowest of these canals, Canale Traverso, is located centrally in what was the capital city's commercial hub and contains a continuous harbor depositional record with average sedimentation rates greater than 1 cm per year. Here we use piston coring, high-resolution core scanning and a multi-proxy sediment analysis including for the first time paleo- and rock-magnetism, and bulk and clay mineralogy in order to overcome the problems of dating harbour deposits and correlating their stratigraphy. The method allowed precise identification of major reworked events, including a dredged deposit and a hyperpycnal deposit, which improve the chronostratigraphy and water depth reconstruction, and sheds light on harbour technologies at the height of the Roman Empire. A debris layer with abundant ceramic fragments and rocks marks the decommissioning of Canale Traverso and provides a new chronostratigraphic marker at Portus. Multi-proxy riverine input signatures point to the possible use of canal gate technology for water flow management.

1 1. INTRODUCTION

2
3 Ancient harbour deposits around the Mediterranean Sea have high accumulation rates of up to one
4 to four centimeters per year (Goiran and Morhange, 2001; Marriner and Morhange, 2006; 2007;
5 Morhange and Marriner, 2010; Goiran et al., 2010; Salomon et al., 2012), which is orders of
6 magnitude higher than in most natural environments such as lakes and oceans (Sadler, 1981). As
7 such, ancient harbour sediment archives can potentially provide high-resolution sedimentary
8 records. With time resolution comparable to varved lake sediment and ice core palaeoclimate
9 records, ancient harbour archives also have the advantage of abundant historical reports. The high
10 time resolution of ancient harbour archives is of interest across disciplines for documenting human-
11 environment interaction, palaeoclimate and history, as well as geomagnetic field change. Such
12 records could, for example, allow further investigation of hypothesised and debated links between
13 climate stability and Roman Empire expansion and contraction (e.g., Büntgen et al., 2011;
14 McCormick et al., 2012; Mensing et al., 2015).

15 Dating is a major challenge that impedes most interpretations of ancient harbour archives. It is
16 challenging because of the large uncertainty of radiocarbon dating and calibration relative to the
17 short time periods covered by ancient deposits, which typically do not exceed several hundred years
18 (e.g., Goiran and Morhange, 2001; Salomon et al., 2012). Dating also depends on the available
19 artefacts, if any, found within the stratigraphy, such as ceramic fragments that can be associated
20 with a specific period. Most importantly, possible dredging of ancient harbour infrastructure
21 significantly complicates attempts to build precise chronologies (Salomon et al., 2016). Historical
22 reports and geoarchaeological evidence indicate that mechanical mud removal was performed to
23 maintain sufficient draught for boats to navigate waterways since the 4th century BC, and more
24 extensively during the Roman Empire (Morhange and Marriner, 2010). Dredging boats unearthed in
25 Marseille constitute direct archaeological evidence for that technology (Pomey, 1995). Further
26 stratigraphic evidence also exists such as a cut-and-fill talus exposed during excavation in

27 Marseilles (Morhange et al., 2003), and wedged scars in volcanic tufa bedrock in the ancient
28 harbour of Naples (Morhange and Marriner, 2010). In sediment cores, however, dredging is at best
29 tentatively identified from radiocarbon date inversions and chronological hiatuses (e.g., Marriner
30 and Morhange, 2006; Marriner et al., 2006; Salomon et al., 2012; Delile et al., 2014; Goiran et al.,
31 2014; Salomon et al., 2016; Stock et al., 2016). Extreme storm, tsunami, and flood events can also
32 cause chronological hiatuses and ‘instantaneous’ deposition (St-Onge et al., 2004; Goiran et al.,
33 2014; Vött et al., 2014; Hadler et al., 2015; Rübke and Vött 2017).

34 Canal gates represent another technology that may have affected sedimentation, but for which
35 evidence is elusive. Historical reports indicate that canal gates may have been used for flood
36 control, navigation or protection (Plinius (nat. hist. III 9,53); Bockius, 2014), yet direct physical
37 evidence is limited to rocky ancient Mediterranean harbours, where rock walls have man-made
38 cuttings (Allen, 1853; McCann, 1979; Erol and Pirazzoli, 1992). Without precise identification of
39 dredging events, extreme weather events, canal gate use, and associated chronological hiatuses
40 and/or reworked deposits within a sedimentary sequence, a precise age-depth model cannot be
41 obtained. Precise identification of event deposits in lake and marine sediment archives is commonly
42 achieved using piston coring to recover the most undisturbed stratigraphy, and high-resolution
43 sediment analysis such as core scanning and magnetic properties (e.g., Duchesne et al., 2006;
44 Storen et al., 2010; Gilli et al., 2013). There are no universal criteria to identify what caused event
45 deposits, and consideration of the local setting and a multi-proxy approach are important. Expected
46 sedimentological evidence for dredging includes sharp contacts, sedimentary discontinuities, and
47 age hiatuses from removal of dredged sediment, and possibly disturbed stratigraphy and mixing of
48 sediment layers from shoveling. In contrast, hydrodynamic high-energy storm, tsunami, flood, and
49 canal gate control events would likely produce graded beds from changes in flow intensity and
50 sediment transport capacity. Event deposits must be taken into account to build robust age-depth
51 models.

52 Portus, the ancient harbour of Rome, is one of the best-studied ancient harbour sites (Keay et al.,
53 2005; Keay and Paroli, 2011). The Emperor Claudius initiated Portus' construction in AD 42 near
54 the Tiber River mouth on the Tyrrhenian Sea, with a second phase of development under the
55 Emperor Trajan (AD 112-117) (Keay et al., 2005), which included construction of the emblematic
56 hexagonal basin that is visible today (Fig. 1). Portus was a large harbour complex that served as the
57 commercial hub and store for Rome at the height of the Roman Empire, receiving goods from all
58 around the Mediterranean Sea. Today, remains of Portus are landlocked three kilometers from the
59 coastline, with part of the port complex lying under the Leonardo da Vinci-Fiumicino International
60 Airport. With exceptionally high sedimentation rates in its basins and canals (Giraudi et al., 2009;
61 Goiran et al., 2010; Salomon et al., 2012; 2014, Delile et al., 2014), the sedimentary archive of
62 Portus has the potential to provide high-resolution geoarchaeological, palaeoclimatic and
63 paleomagnetic records. No previous study has provided precise chronologies because of: 1) the
64 disturbed stratigraphy of cores that were drilled using rotating core barrels and extraction of
65 sediment into plastic trays; 2) possibly unidentified hiatuses and/or event deposits; and 3) large
66 radiocarbon dating and calibration uncertainties relative to the short period covered by the harbour
67 deposit. As a result, age-depth models from Portus are mostly vertical with several meters of mud
68 having the same age, and the stratigraphy of cores is difficult to correlate to each other. At Portus,
69 sedimentary radiocarbon date inversions provide hints of dredging (Delile et al., 2014; Salomon et
70 al., 2012; Goiran et al., 2010) and dredging in Portus basins is depicted in an epigraph at ca AD 400
71 (Coccia, 1993; Giraudi et al., 2009). Flood gates or canal locks were also hypothesised on the canals
72 of Portus, including the Canale Traverso (Testaguzza, 1970), the Fossa Traiana, and the Canale
73 Romano (Salomon et al., 2014); however, there has been no conclusive evidence for these
74 technologies. Portus was clearly influenced by fluvial input however, no flood layer has been
75 identified (Salomon et al., 2012; 2014). Flood and/or storm/tsunami deposits have been reported in
76 the harbour of Ostia, also located on the Tiber delta, in the centuries preceding the construction of
77 Portus (Goiran et al, 2014; Hadler et al, 2015; Marriner et al, 2017). Here we apply methods

78 commonly used in marine geology, including piston coring, high-resolution core scanning, and
79 multi-proxy sediment analyses (grain size, paleo- and rock-magnetism, and bulk and clay
80 mineralogy), together with radiocarbon dating and Bayesian age modelling to precisely identify
81 event deposits and to better constrain the Portus chronostratigraphy, and to document Roman
82 harbour technologies.

83 2. MATERIAL AND METHODS

84 2.1 Field Work

85 Coring operations were completed in September 2011 using a stationary hydraulic piston system
86 operated by the *Centre d'Étude Techniques de l'Équipement (CETE) Méditerranée*. This method
87 allows recovery of relatively undisturbed and continuous sediment sequences with core sections
88 preserved in polyvinyl chloride (PVC) tube liners. The cores were sealed and shipped to the *Institut*
89 *des sciences de la mer de Rimouski (ISMER)* of the *Université du Québec à Rimouski (UQAR)* for
90 analysis. Based on the high sediment accumulation rates (Salomon et al., 2012) and the results of a
91 pilot rock-magnetic study (cf. section 2.2) it was decided to core Canale Traverso. The coring site in
92 Canale Traverso was selected near the access channel (Fig. 1B) based on the hypothesis that the
93 hydraulic energy would dissipate and, thus, sediment would accumulate most rapidly where canal
94 widens. Two cores, CPS1 and CPS4, were recovered from that location (Figs. 1B, D). CPS1 was
95 selected for high-resolution multi-proxy study because of its thicker apparent harbour deposit.

96 2.2 Pilot Study

97 Samples from previous rotary drilling at Portus (Goiran et al., 2010; Salomon et al., 2012) were
98 analysed at ISMER prior to field work to evaluate the potential for paleo- and environmental
99 magnetism studies at Portus. Eight sediment samples were chosen from core TR-20 in the access
100 channel and seven samples from core CT1 in Canale Traverso (see core locations in Fig. 1B). The
101 performed analyses include temperature dependence of magnetic susceptibility (50 to 700 °C),
102 alternating field (AF) demagnetisation of the natural remanent magnetisation (NRM), hysteresis
103 properties, and isothermal remanent magnetisation (IRM) acquisition (methods summarized in Lisé-

104 Pronovost et al., 2013). Results of the pilot study (supplementary material 1) indicate that Canale
105 Traverso was the most promising site with a strong magnetic signal dominated by low coercivity
106 magnetite with single domain (SD) to vortex magnetic state, and a stable NRM, which are suitable
107 for paleomagnetic recording (Tauxe, 1993). By comparison, sediment from the access channel (TR-
108 20) has a weak magnetic signal likely associated with dissolution of detrital ferrimagnetic particles
109 in less oxygenated and more organic-rich sediment (e.g., Roberts, 2015), because the site is located
110 further away from fluvial input to the harbour.

111 2.3 High-Resolution Analyses

112 Magnetic, physical, and mineralogical analyses of core CPS1 were undertaken at high-resolution on
113 whole core sections, on half-core split surfaces, on continuous u-channels (2 cm x 2 cm x core
114 length), and on a series of discrete samples (Table 1). The discrete samples are a series of 50
115 standard 8 cm³ cubes (2 cm x 2 cm x 2 cm) that were used for magnetic analysis and ca 5 g of
116 sediment that was used for mineralogical analysis, taken at ca 10 cm intervals down-core (see
117 sampling strategy log in Fig. 2). This discrete sampling interval is comparable to the highest
118 sampling resolution previously achieved in Portus.

119 2.3.1 Physical Properties

120 CT-scan images and gamma ray attenuation provide indications of sediment density. They are
121 measured rapidly at high-resolution and are non-destructive (St-Onge et al., 2007; Fortin et al.,
122 2013). CT-scan images of whole cores was obtained at the *Institut national de la recherche*
123 *scientifique Eau-Terre-Environnements* (INRS-ETE) using a Siemens SOMATOM Definition sliding
124 gantry CT-Scanner. Tomograms were acquired continuously with a pixel size of 0.06 cm and were
125 then transferred into digital format using a standard Hounsfield scale (Hounsfield, 1973). Higher
126 density and higher atomic numbers generate greater X-ray attenuation, which is represented by
127 higher CT number and lighter tones on a CT scan image. Gamma ray attenuation was measured on
128 whole cores at 1-cm intervals using a Cesium-137 gamma ray source and detector mounted on a

129 multi-sensor core logger (MSCL; Geotek Ltd.) at ISMER, UQAR. Imaging of half-core split
130 surfaces was done using a linescan imaging Geoscan IV (Geotek Ltd) instrument.

131 2.3.2 Magnetic Properties

132 Magnetic mineral assemblages in the sediment were characterised using room-temperature
133 magnetic properties, including the magnetic susceptibility, NRM and laboratory-induced
134 magnetisations, and coercivity-dependent parameters. Magnetic susceptibility primarily reflects
135 ferrimagnetic mineral concentration and is influenced by sediment composition, magnetic
136 mineralogy, and grain size. The volume magnetic susceptibility (κ) was measured on the whole
137 cores using a Bartington Instruments MS2C loop sensor at 1-cm stratigraphic intervals, and then on
138 the half-core split surface with a MS2E high-sensitivity point sensor at 0.5-cm stratigraphic
139 intervals at ISMER. Frequency-dependent magnetic susceptibility ($\chi_{FD\%}$) of cube samples was
140 measured using a MS2B dual frequency sensor at The Australian Archaeomagnetism Laboratory
141 (TAAL), La Trobe University. $\chi_{FD\%}$ is defined as $\chi_{FD\%} = (\chi_{LF} - \chi_{HF}) / \chi_{LF} \times 100$, with low and high
142 frequencies (LF and HF) of 0.46 and 4.6 kHz, respectively (Dearing, 1999). $\chi_{FD\%}$ is controlled by
143 the grain size distribution of superparamagnetic (SP) and stable SD particles (Eyre, 1997).
144 Measurements were repeated at least six times; average values and standard errors are reported.

145 The NRM and ARM were measured and stepwise demagnetised on u-channels from 0 to 100 mT in
146 13 and 5 steps, respectively, using a 2-G Enterprises cryogenic magnetometer for u-channels at
147 ISMER. ARM was imparted in a peak AF of 100 mT with a direct bias field of 0.05 mT. κ_{ARM} is the
148 ARM normalised by the direct bias field. Principal component analysis (PCA) of NRM
149 demagnetisation data was performed using the Puffin Plot software (Lurcock and Wilson, 2012).
150 Four data points were masked at section ends to account for the width of the response function of
151 the cryogenic magnetometer pick-up coils (Weeks et al., 1993) and data from intervals with
152 incompletely filled u-channels or gaps were removed. The median destructive field (MDF) is the
153 AF required to demagnetise half of the initial remanence. MDF is a coercivity indicator and is a
154 useful grain size indicator when the magnetic mineral assemblage is uniform (Dankers, 1981;

155 Dunlop and Ozdemir, 1997). Like κ , ARM is controlled mainly by the concentration of
156 ferrimagnetic particles. In addition, SD grains more easily acquire ARM than coarser multi-domain
157 (MD) grains (Maher, 1988; Evans and Heller, 2003), so ARM is also a useful magnetic grain size
158 indicator (i.e., κ_{ARM}/κ , MDF_{ARM}).

159 Hysteresis loops, IRM acquisition curves, and backfield demagnetisation curves were measured for
160 each sample in a maximum field of 1 T using a Princeton Measurement Corp. vibrating sample
161 magnetometer at the Australian National University (ANU). The bulk coercive force (H_c), the
162 remanent coercive force (H_{cr}), the saturation magnetisation (M_s), and the saturation remanence (M_r)
163 were obtained and the ratios M_r/M_s and H_{cr}/H_c are used as magnetic grain size indicators (Day et al.,
164 1977). The hard isothermal remanent magnetisation ($HIRM = (IRM_{1T} + IRM_{0.3T})/2$; King and
165 Channell, 1991) and the S-ratio ($S\text{-ratio} = -IRM_{-300mT}/SIRM$; Stober and Thompson, 1979) were
166 calculated; they reflect the absolute concentration of high coercivity magnetic minerals and the
167 relative concentration of low to high coercivity minerals, respectively (Liu et al., 2012). $B_{1/2}$ is half
168 the applied field required for a sample to reach saturation and reflects the ease with which a sample
169 is magnetised; it is a coercivity indicator. The 50 measured IRM acquisition curves were unmixed
170 using an unsupervised approach (Heslop and Dillon, 2007) to identify and characterise the end-
171 members that represent magnetic grain populations. Finally, first-order reversal curve (FORC;
172 Roberts et al., 2000) diagrams for seven samples (CPS1-3-7, 4-5, 4-11, 5-5, 5-8, 6-8, and 7-3) were
173 obtained using the same instrument to further explore the magnetic coercivity spectrum, domain
174 structure, and magnetic interactions of different sediment types.

175 2.3.3 Granulometry

176 After completion of magnetic analyses, sediments in cube samples were air-dried at room
177 temperature. To prepare samples for grain size analysis, dried sediments were sieved through a 2-
178 mm mesh and were gently homogenised using an agate mortar and pestle. Subsamples of about 2 g
179 were treated repeatedly with hydrogen peroxide (H_2O_2) and gentle heating to remove organic
180 matter, until peroxide addition to the sediment did not react further. Finally, sediment dispersion of

181 the treated and rinsed samples was achieved by adding 1 mL of 0.5M sodium hexametaphosphate
182 (NaPO_3) and ultrasonicated for 15 minutes. Grain size analyses were performed using a Malvern
183 Mastersizer 2000 laser diffraction spectrophotometer at the Australian Nuclear Science and
184 Technology Organisation (ANSTO). Each prepared sample underwent three successive 10-second
185 measurement runs using continuous sonication to disperse aggregated particles. All statistical grain-
186 size parameters were calculated with the GRADISTAT software (Blott and Pye, 2001) using the
187 Folk and Ward graphical method (Folk and Ward, 1957). Logarithmic biplots of the median (D50)
188 and 90th percentile diameter (D90) or the Passega diagram (Passega, 1964; Bravard and Peiry,
189 1999) were used to estimate the hydrodynamic energy associated with sediment deposition from
190 decantation to rolling.

191 2.3.4 Bulk and Clay Mineralogy

192 Before mineralogical analysis, the detrital sediment fraction of the samples was isolated using 10
193 mL of peroxide (30% H_2O_2) and 10 mL of hydrochloric acid (0.5M HCl) to remove organic matter
194 and biogenic carbonate, respectively. Deflocculation was achieved by successive washings with
195 distilled water. Next, for bulk mineralogy, sediment samples were ground with a McCrone
196 micronizing mill with agate grinding elements for 5-10 min with 10 mL of ethanol to obtain a
197 consistent grain size of $<10 \mu\text{m}$. The slurry was oven dried overnight at 60°C and was slightly
198 homogenised with an agate mortar to avoid agglomeration of finer particles during drying. Random
199 powder samples were analysed by X-ray diffraction (XRD) using a PANalytical X'Pert Powder
200 diffractometer (copper anode; 45 kV; 40 mA intensity). Samples were scanned from 5° to 65° two-
201 theta in steps of 0.020° two-theta and a counting time of 2 seconds per step.

202 For semi-quantification of major mineralogical components, bulk sediment XRD scans were
203 processed using the software package X'Pert High-Score Plus (PANalytical) with Rietveld full-
204 pattern fitting. This method permits semi-quantification of whole-sediment mineralogy with a
205 precision of 5–10% for phyllosilicates and 5% for grain minerals. Major mineralogical components
206 quantified by this technique are quartz, K-feldspar, plagioclase feldspar, pyroxene, magnetite,

207 pyrite, and phyllosilicates. The sum of quartz, phyllosilicates, K-feldspar, and Na-plagioclase
208 contents is a detritus index that reflects changes in detrital influx or terrigenous supply (e.g., Keller
209 and Pardo, 2004; Mort et al., 2008; Montero-Serrano et al., 2015). The ratio of fine detrital material
210 (phyllosilicates) to coarse detrital material (quartz, plagioclases, and K-feldspars) is denoted
211 $Phy/(Qz+Pl+Feld)$ and indicates hydrodynamic sorting intensity.

212 Clay-mineral associations (smectite, illite, kaolinite, and chlorite) were studied using XRD
213 following the protocols of Bout-Roumzeilles et al. (1999) and Montero-Serrano et al. (2009). The
214 clay fraction was separated by settling according to Stokes's law, concentrated by centrifugation,
215 and oriented by wet smearing on glass slides. Analyses were run from 2.49° to 32.49° 2θ on a
216 PANalytical X'Pert Powder diffractometer. Three runs were made after air-drying each sample with
217 ethyleneglycol vapour saturation for 12 hours and heating at 490°C for 2 hours. Each clay mineral
218 is characterised by its basal layer plus interlayer interval (d) from XRD analysis (Brown and
219 Brindley, 1980). Semi-quantitative clay mineral abundance estimation (smectite, illite, chlorite, and
220 kaolinite), based on peak areas, was performed using the MacDiff® 4.2.5 software (Petschick,
221 2000). The reproducibility of measurements is estimated to be 5% for each clay mineral, as checked
222 by replicate sample analysis.

223

224 2.3.5 Radiocarbon dating

225 Radiocarbon dating was performed using an Accelerator Mass Spectrometry (AMS) at ANSTO
226 (Fink et al., 2004). Six samples of short-lived terrestrial material were measured, including three
227 seeds, one coniferous bud, and two pollen/charcoal samples (Table 2). Measured ages were
228 calibrated using the ^{14}C calibration program CALIB 7.0 (<http://calib.qub.ac.uk/calib/calib.html>; 1.0
229 (Stuiver et al., 2017) and the IntCal13 dataset (Reimer et al., 2013) and are stated using 2 sigma
230 errors. The pollen extraction by density separation with lithium heteropolytungstate (LST) heavy
231 liquid revealed abundant charcoal in the two pollen samples, and charcoal could not be separated
232 from the pollen prior to dating. The dated carbon for samples OZS598 and OZS602 must, thus,

233 come from both pollen and charcoal with possibly different respective ages. This was taken into
234 account using Bayesian age modelling with the Charcoal Outlier Model in OxCal v4.2.3 (Bronk
235 Ramsey and Lee, 2013), with an overall agreement of 93%. This model considers sample types and
236 for the two pollen samples that also incorporated charcoal, outliers to older times are allowed to
237 account for possible older wood in charcoal. The same radiocarbon calibration and age modelling
238 method was applied to previously published radiocarbon dates from Portus cores TR14 (Delile et
239 al., 2014) and CT1 (Salomon et al., 2012).

240 3. RESULTS

241 3.1 Stratigraphy

242 Six sedimentary units, labelled A to F from base to top, are defined based on lithology from core
243 descriptions, photos, CT-scanning, density (gamma-ray attenuation and CT-number), magnetic
244 susceptibility, and physical grain size data (Fig. 2). These units are described as follows.

245 3.1.1 Unit A

246 Unit A occurs at the base of the core (696 cm) to 573 cm and is composed of laminated yellow
247 muddy sands characterised by relatively high density and magnetic susceptibility values (Fig. 2).
248 Grain size analysis of four discrete samples indicate unimodal distributions and mean grain size
249 ranging from 47 to 119 μm . The upper 10 cm has fine laminations of sandy muds and muddy sands.
250 A sharp oblique discontinuity cuts these laminations and marks the end of unit A. Unit A has
251 relatively high quartz content (up to 45%), coarse detrital material (Phy/(Qz+Pl+Feld)), and
252 virtually no pyrite or pyroxene (Fig. 3). The magnetic particle assemblage is dominated by low
253 coercivity minerals, as indicated by saturation of the IRM below 300 mT, which results in S-ratio
254 values close to one and low HIRM values (Fig. 3). The low-coercivity magnetic component EM1
255 has the highest relative contribution in unit A, reaching 86% of the IRM (Fig. 3).

256 3.1.2 Unit B

257 Unit B is identified from depths of 573 to 480 cm and is composed of massive sands and muddy
258 sands with cm-sized mud clasts. Immediately above the sharp oblique discontinuity at 573 cm is a
259 38-cm-thick massive medium sand layer with unimodal grain size distribution (mode 340 μm ;
260 sample 7-1; Fig. 2E) that encompasses the coarsest mean grain size in the studied core CPS1 (291
261 μm ; sample 7-1; Fig. 2E). At 535 cm, a sharp κ drop of one order of magnitude and an increased
262 mud content marks a change from sand to muddy sand (Figs. 2C-D). The muddy sand has a
263 bimodal grain size distribution, with a first mode similar to the massive sand (341 μm) and a much
264 finer second mode of 39 μm (each mode is calculated from 4 samples). Sample 6-8 was taken from
265 an individual mud clast within the muddy sands and is a distinctly finer medium silt with mean
266 grain size of 8 μm (Fig. 2E). Unit B is clearly composed of ungraded reworked sediments. This unit
267 is capped with fine laminations of very coarse silts (mean grain size of 47 μm ; sample 6-5). The
268 mineralogical and magnetic properties in the massive sands of unit B are similar to these of unit A.
269 In contrast, the muddy sands with mud clasts in unit B have relatively lower quartz content (30 to
270 34%), finer detrital minerals ($\text{Phy}/(\text{Qz}+\text{Pl}+\text{Feld})$), and higher pyrite (0.5 to 1.4%) contents (Fig. 4).
271 The magnetic component EM2 appears in unit B and reaches maximum values in mud clast sample
272 6-8 (Fig. 4).

273 3.1.3 Unit C

274 Unit C from 480 to 414 cm is composed of graded beds of muddy sands and sandy muds
275 intercalated with a 30-cm-thick central layer (430-460 cm) of abundant cm-size rocks, ceramic
276 fragments, wood, and other organic debris. A sharp change in gamma ray attenuation and CT-
277 number at 480 cm (Fig. 2A-B) reflects the distinct densities of sedimentary units B and C. The grain
278 size distributions of the six discrete samples from unit C reveal, from base to top, a coarsening
279 upward sequence and a fining upward sequence. Similarly, the concentration of ferrimagnetic
280 minerals as indicated by κ , M_s , ARM, and NRM increases steeply from the base of unit C to the
281 debris layer, and decreases gradually to the top of unit C. The three samples within the debris layer

282 have trimodal grain size distributions with the coarser mode reaching 590 μm (Fig. 2E). In contrast,
283 samples below and above the debris layer have bimodal distributions (224 and 6 μm). Mineralogical
284 and magnetic properties have sharp and large amplitude changes in the debris layer of unit C.
285 Notably HIRM, magnetic component EM1, and the pyroxene content reach peak values (Fig. 3). In
286 addition, paleomagnetic inclinations depart markedly from the expected value for a geocentric axial
287 dipole (GAD) field at the latitude of the coring site. Instead of dipping 61° below the horizontal
288 plane, the magnetic inclination is flattened horizontally and has reversed polarity.

289 3.1.4 Unit D

290 Unit D is from 414 to 165 cm and is the thickest and most homogenous sedimentary unit of core
291 CPS1. The base of unit D is characterised by a sharp increase in mud content from 44% (sample 5-8
292 at 423 cm in unit C) to 86% (sample 5-7 at 413 cm in unit D). Overall, unit D has lower amplitude
293 variations in density, magnetic susceptibility, and mud content (Fig. 2). Two sub-units D1 (414-220
294 cm) and D2 (220-165 cm) are identified. D1 is composed of medium silts with average grain size of
295 $13 \pm 3 \mu\text{m}$ (19 samples) and unimodal grain size distributions (Fig. 3E). D1 has virtually no
296 particles bigger than 2 mm. In contrast, sub-unit D2 (6 samples) has particles over 2 mm and
297 organic debris, it is composed of coarsening upward coarse to very coarse silts with average grain
298 size of $30 \pm 4 \mu\text{m}$, and grain size distributions are bimodal at the base and trimodal at the top (Fig.
299 2E). Unit D has distinctively finer detrital minerals (Phy/(Qz+Pl+Feld)), relatively higher pyrite and
300 gypsum contents, and lower S-ratios than the other units (Fig. 3), and there are three magnetic grain
301 populations (Fig. 4). The two sub-units have remarkably different mineralogy and magnetic
302 properties. The detrital minerals are much coarser in sub-unit D2 than D1, and the quartz content
303 increases from 29% to 36% (Fig. 3). Sub-unit D2 has peak values of HIRM, EM1, and pyroxene;
304 the same signature occurs in the debris layer of unit C and is found in overlying unit E (Fig. 3).
305 Moreover, in sub-unit D2 the magnetic grain size indicators M_r/M_s , H_{cr}/H_c , MDF_{ARM} , χ_{FD} (Fig. 5)
306 and the open shape of hysteresis loops (supplementary material 3) all indicate smaller ferrimagnetic
307 grains.

308 3.1.5 Unit E

309 Unit E from 165 to 50 cm is composed of abundant potshards and shell fragments, rocks, and
310 organic debris associated with large amplitude changes in density, magnetic susceptibility, and mud
311 content (Fig. 2). The irregular surface of the debris-dominated unit E prevented the use of the multi-
312 sensor core logger for core section 2. U-channel sampling was also impossible with many debris
313 pieces being larger than the u-channel width (2 cm). Nevertheless, the four discrete sediment
314 samples analyzed for granulometry are coarse silts to fine sands with highly variable average grain
315 size (ranging from 23 to 158 μm) and uni- to tri-modal grain size distributions. Magnetic
316 mineralogy and grain size are also variable (Figs. 3 and 5). There is a trend toward finer detrital
317 minerals and the pyrite content decreases sharply to minimum values (Fig. 3). Magnetic component
318 EM2 has maximum values (Fig. 4), with χ_{fd} values from 3 to 7 being indicative of fine SD and SP
319 grains.

320 3.1.6 Unit F

321 The uppermost unit F from 50 to 0 cm is composed of silts with a color transition from yellow to
322 brown. The yellow mud has unimodal grain size distribution and average grain size of 9 μm
323 (sample 1-2; Fig. 2E). The brown mud has a trimodal distribution and average grain size of 19 μm
324 (sample 1-1). Magnetic component EM1 dominates with values up to 79%, similar to unit A.

325 3.2 Magnetic Mineral Assemblage

326 Magnetic properties provide information about the nature, source, and transportation of magnetic
327 particle populations in a sediment. The studied bulk sediment is dominated by low coercivity
328 magnetic minerals, as indicated by IRM saturation in fields below 300 mT (Fig. 4). FORC diagrams
329 (supplementary material 3) and $\chi_{FD\%}$ values (Fig. 5) indicate a mixture of SD, MD, and SP domain
330 states. MDF_{ARM} has the same general down-core trend as $\chi_{FD\%}$ and values (32 to 40 mT) are
331 consistent with those of detrital and low coercivity biogenic magnetic minerals (Egli, 2004).
332 Ultrafine SP particles form commonly in soils and by burning (Evans and Heller, 2003; Herries,
333 2009), the latter being likely in Portus from cooking and heating.

334 Unmixing analysis of 50 IRM acquisition curves (Heslop, 2015) indicates that there are three end-
335 members (EM1, 2 and 3; Fig. 4) with the fit yielding an R^2 value of 0.988. The three magnetic
336 subpopulations EM1, EM2, and EM3 have coercivities ($B_{1/2}$; Fig. 4) of 21, 31, and 11 mT,
337 respectively. The proportion of the higher coercivity population EM2 is greater in muddy sediments
338 (units C, D, E), while the intermediate coercivity EM1 component has peak values in sandy deposits
339 (units A, B, F). Peak concentrations of EM1 also correspond to lower relative contributions from
340 the other magnetic component (Fig. 4), which hints at a sudden input of EM1. Moreover, EM1
341 peaks are associated with peak pyroxene contents (Fig. 3), which likely come from basalts in the
342 Tiber River catchment; peak HIRM values (Fig. 3) may also correspond to inputs of these volcanic
343 grains, or to pedogenic magnetic minerals such as goethite and hematite brought by runoff.
344 Altogether, the magnetic properties suggest that EM1 corresponds to detrital magnetic minerals of
345 fluvial origin and that EM2 corresponds to biogenic magnetic minerals from the harbour. The
346 lowest coercivity population EM3 is present in lower proportions (generally $< 30\%$; Fig. 4), with
347 higher absolute values in the sands of units A and B (not shown), and hysteresis loops, coercivity
348 ratios, and remanence ratios indicative of MD magnetic minerals.

349 3.3 Chronology

350 Radiocarbon dating, calibration, and Bayesian depth-age modelling reveals two distinct periods in
351 core CPS1 (Fig. 6; Table 2). The first period corresponds to sandy unit A in the lower portion of the
352 core and has one date (calibrated 765-492 BC; modelled 764-434 BC). The second period
353 corresponds to homogeneous muddy unit D (414-165 cm) and comprises four dates between cal AD
354 28 and AD 311. Another date from the upper part of the high-energy flow deposit (unit C) is
355 derived from extracted pollen/charcoal (sample OZS598) and gives a large modelled age
356 uncertainty (Table 2) because of the presence of charcoal from burnt material with a possible
357 inherited age. Sub-centimeter-sized ceramic fragments in the central layer of the high-energy flow
358 deposit (unit C) indicate human activity and provide some chronological insight. The small ceramic

359 fragments have similar color and texture to those in the uppermost debris layer (unit E) that caps the
360 harbour deposit (unit D).

361 The four dates in homogeneous unit D reveal rapid sediment deposition during the Roman Empire.
362 The calibrated radiocarbon dates fall within the interval cal AD 28 – AD 311, and Bayesian age
363 modelling, which takes into account the type of dated material, gives slightly younger probable
364 dates and a larger age interval AD 128 – AD 616 because the uppermost sample OZS602 consists
365 of a pollen/charcoal mixture (Table 2; Fig. 6). The radiocarbon-based chronology of unit D assumes
366 constant sedimentation rates (linear interpolation) between the median modelled ages (Table 2) and
367 suggests deposition over 165 years during the second and third century AD, at average
368 sedimentation rates of ~1 cm per year (Fig. 6B). The true harbour deposition period could be shorter
369 or longer than suggested by age modelling because of the uncertain uppermost date. The harbour
370 deposit period is short relative to radiocarbon dating and calibration errors, and therefore the
371 radiocarbon-based chronology cannot be used to date historical events. Instead, the core CPS1
372 chronology provides a detailed sequence of events. Each cm of muddy unit D in core CPS1
373 integrates on average less than one year, and each cube sample no more than 2 years.

374 4. DISCUSSION

375 4.1 High-resolution chronostratigraphy of core CPS1

376 The often complex stratigraphy of ancient Roman harbours (e.g., Hadler et al., 2015; Finkler et al.,
377 2017) can be simplified to a three-unit sequence: a pre-harbour deposit, a harbour deposit, and a
378 post-harbour or abandonment deposit (e.g., Goiran and Morhange, 2001; Marriner and Morhange,
379 2007). The same general stratigraphy is reported here from the first stationary piston core recovered
380 from Portus, and the new core chronostratigraphy is interpreted based on high-resolution multi-
381 proxy analysis, age modelling, and historical context.

382 In core CPS1, the *pre-harbour deposit* corresponds to unit A and consists of stratified fluvio-coastal
383 sediments. The smaller grain sizes and fine laminations in the upper part of unit A indicate calmer
384 hydrological conditions possibly associated with a fluvial or lagoon environment. The radiocarbon-

385 dated seed from the uppermost laminations of unit A yield an age (Table 2; Fig. 6A) consistent with
386 previous geomorphological and stratigraphic studies that indicate that the Tiber River mouth was
387 located near the site in the first millennium BC (Bellotti et al., 2011; Giraudi et al., 2009).

388 The *harbour deposit* consists of unit D and covers a continuous period of about one and a half
389 centuries (Fig. 2B). The distinctive sedimentological signature of the harbour deposit relative to the
390 natural pre-harbour deposit is evident from granulometry, physical and magnetic properties, bulk
391 sediment, and clay mineralogy data (Figs. 2, 3, 4). The harbour deposit in the man-made Canale
392 Traverso is characterised by greater mud content and finer detrital minerals (Fig. 3) that indicate a
393 calmer, more isolated depositional environment. Relatively higher pyrite contents, lower
394 ferrimagnetic mineral concentrations (lower κ , M_s , NRM, ARM), and the presence of biogenic
395 magnetite (EM2; Fig. 4) indicate a more organic-rich deposit and more hypoxic conditions. An age
396 for the start of the harbour deposit in Canale Traverso core CPS1 is obtained by interpolation and is
397 modelled at AD 120 – AD 186 (Fig. 6). This age estimate suggests that the onset of harbour
398 deposition in core CPS1 followed the massive enlargement and reorganization of Portus by Trajan
399 that was completed by AD 117 (Keay et al., 2005). However, it is believed that Canale Traverso
400 was built earlier, during the first century AD, as part of the initial Claudius harbour construction.
401 This is based on the hypothesis of Testaguzza (1970) who suggested that the Darsena, Canale
402 Traverso, and Fossa Traiana formed a complex built at the same time, and on the radiocarbon
403 chronology of Canale Traverso core CT1 that contains sediment from the first century (Salomon et
404 al., 2012). If the Canale Traverso was built during the first century AD, the age of the basal harbour
405 deposit in core CPS1 does not date construction of Canale Traverso, but rather indicates that
406 dredging operations removed about one century of previous harbour deposit. This issue is
407 considered in section 4.3. The modelled age for the end of harbour deposit is obtained by
408 interpolation at AD 164 - AD 643 (Fig. 6). The large age interval is inherent to the nature of the
409 dated material (charcoal-rich pollen sample OZS602). Nevertheless, the modelled age interval AD

410 177 - AD 436 is obtained if sample OZS602 is not considered and a constant sedimentation rate is
411 assumed from sample OZS601 to the top of the harbour sequence (Fig. 6).

412 Units E-F represent the *post-harbour deposit*. Accumulation of debris (unit E) into Canale Traverso
413 marked the end of its use as a waterway. Uppermost unit F includes floodplain deposits and the
414 recent soil deposit. What stands out in the stratigraphy of core CPS1 are the two consecutive
415 reworked deposits (units B and C) located between the pre-harbour and harbour deposits. For the
416 first time at Portus, reworked layers are identified precisely using high-resolution core scanning and
417 multi-proxy analyses. Units B and C are discussed in more detail below.

418 4.2 New Chronostratigraphic Marker

419 The estimated end of harbour deposition in Canale Traverso is consistent with dates from cores S13
420 and TR14 located downstream in the access channel (70 m and 170 m distance from CPS1; Fig 1B),
421 but is significantly younger than in core CT1, which is located upstream toward Fossa Traiana (130
422 m distance from CPS1; Fig. 1B). Based on grain size data in core CT1, Salomon et al. (2012)
423 reported two distinct harbour deposits; one with low Tiber River influence and one with high Tiber
424 River influence (Fig. 7; Salomon et al., 2012). Our pilot magnetic analysis supports this stratigraphy
425 with a distinct magnetic mineral assemblage in the core CT1 high Tiber River influence deposit and
426 similar magnetic assemblages for the CT1 low Tiber influence deposit and core TR20 from the
427 access channel (supplementary material 1). The sudden change in CT1 sediment type corresponds
428 to a sharp κ increase, which can be correlated to a similar sharp κ increase at a similar median
429 modelled age in core CPS1 (Fig. 7). While the sharp κ increase in core CT1 likely corresponds to
430 increased river transport of ferrimagnetic detrital particles, the sharp κ increase in core CPS1
431 corresponds to the debris layer (unit E; Fig. 2), which also has large amplitude changes attributed to
432 abundant ceramic fragments, rocks, and overall heterogeneous debris having highly variable
433 magnetic properties. At a similar modelled age in core TR14, a sudden onset of marine influence is
434 evident in the access channel based on geochemistry data (Fig. 7; Delile et al., 2014). Core CPS1 is
435 located between cores TR14 and CT1 and, thus, provides a link for correlating the Portus cores.

436 Damming of Canale Traverso with debris at the junction of the access channel (site CPS1) would
437 have blocked river input into the harbour basins, changing predominantly fluvial to marine
438 influence in the access channel (TR14), and increasing river influence upstream of Canale Traverso
439 (CT1). Combining age modelling, κ records, and previous grain size and geochemistry studies
440 (Salomon et al., 2012; Delile et al., 2014) reveals a new chronostratigraphic marker at Portus at the
441 time Canale Traverso was decommissioned. This change may correspond to Portus becoming a
442 town in the 4th century when the immediate vicinity of Canale Traverso changed its function from
443 administrative to residential (Keay et al, 2005; Paroli, 2005).

444 4.3 Reworking of Sediments into a Roman Canal

445 4.3.1 The Dredged Deposit

446 CT scan and digital images clearly reveal an oblique erosional contact that cuts natural laminated
447 deposits and is overlain by 93 cm of sands with angular mud clasts in the upper part (unit B; Fig. 2).
448 The sands deposited before and after the oblique contact have similar physical, mineralogical, and
449 magnetic properties (Figs. 2, 3, 4, 5), which suggests that the reworked unit B was sourced locally.
450 The presence of rectangular-shaped mud clasts with immature texture (Lie et al., 2017) further
451 indicates a local mass movement event such as a river bank collapse, a landslide or debris flow,
452 possibly triggered by human activities or an earthquake. However, observed immature mud clasts
453 embedded in much coarser sands imply a local source of mud deposited in a calm environment and
454 a local source of sands deposited in a vigorous hydrodynamic environment. Contemporaneous mud
455 and sand deposits within a small fabricated canal appears unlikely, and a local mass movement is
456 unlikely to explain the oblique erosive contact in the canal center. Another hypothesis is a weather-
457 related event such as storm, tsunami or flood. Such high-energy events have been reported in the
458 nearby Ostia harbour (Goiran et al., 2014; Hadler et al., 2015); whilst event deposits in Portus are
459 reported here for the first time, the river influence at Portus is well-documented (Goiran et al., 2010;
460 Delile et al., 2014; Salomon et al., 2012; 2014). A flood appears likely; however, a high-energy
461 flow is inconsistent with the ungraded sands and immature mud clasts of unit B, which rather point

462 to low velocity flow. A more likely explanation is that unit B corresponds to an admixture of coastal
463 sands and harbour mud that were shoveled locally and dropped into place, forming a dredged
464 deposit (Table 3; Fig. 8). Multi-proxy analyses of the mud clast (sample 6-8) indicate contrasting
465 magnetic and physical properties with the later harbour mud of unit D, which points to different
466 depositional conditions before and after dredging. The differences include distinctively higher S-
467 ratio and higher EM2 biogenic proportion in the mud clast (Figs. 3, 4), and the lowest D50 value of
468 core CPS1, with the grain size of sample 6-8 plotting in the lower energy or decantation end of
469 Figure 5F. It is, thus, possible that dredging was performed at the time of the major Trajan work,
470 which drastically changed the harbour infrastructure (Keay et al., 2005) and hydrodynamics (Millet
471 et al., 2014).

472 Further support for calm hydrodynamic conditions at the time of deposition of unit B comes from
473 the paleomagnetic inclination. Muddy sands in upper unit B have a strong, stable, and well-defined
474 magnetic remanence with inclination values near the GAD field value for the latitude of Portus
475 (Figs. 9D, 10). In unit B, three distinct magnetic particle populations (Fig. 4) form a single
476 magnetization component, which indicates that a detrital remanent magnetisation (DRM)
477 acquisition process at about the time of deposition is more likely than a chemical remanent
478 magnetisation (CRM) that would have happened anytime later. Additional support for a DRM
479 comes from the predominance of biogenic particles in the supposedly dredged deposit because such
480 particles are small and readily undergo chemical alteration. Such rapid remanence acquisition
481 within an event deposit resembles redeposition experiments of slurries with low water content
482 (Barton et al, 1980) and adobe brick fabrication, where clay and water mixtures rapidly acquire a
483 shear or shock remanent magnetisation when thrown into a mould (Games, 1977; 1983). The
484 paleomagnetic results, thus, indicate limited resuspension of slurry material and calm hydrodynamic
485 conditions at the site, which further supports the suggested dredged deposit interpretation for unit B.

486 4.3.2 The Hyperpycnal Deposit

487 Immediately overlying the dredged deposit (unit B) is another reworked deposit of 66 cm thickness
488 (unit C), which is composed of a coarsening upward basal sequence, a 30 cm-thick central debris
489 layer, and a fining upward top sequence. Unit C is a typical hyperpycnite that results from high-
490 energy flow that sorts particles into a coarsening sequence during the waxing stage of the flow, and
491 a fining upward sequence during the waning stage of the flow (Mulder, 2003; Fig. 8). The
492 hyperpycnal deposit in core CPS1 is readily identifiable using grain size, bulk mineralogy, and
493 magnetic data (Fig. 10). In addition to grain size sorting, flattened paleomagnetic inclinations (Figs.
494 9C and 10) are an indicator of high-energy deposits (St-Onge et al., 2004). The distinct sedimentary
495 properties of the central debris layer provide a clear river input signature, particularly using the
496 fluvial magnetic component EM1, the content of high coercivity minerals (HIRM) and pyroxenes,
497 and a higher smectite/(illite+chlorite) ratio (Fig. 3). Coeval peak values of these parameters in the
498 debris layer point to a common fluvial source and transport mechanism for different types of detrital
499 material.

500 Hyperpycnal deposits in natural environments are associated with dense water flowing into less
501 dense water, the most typical example being sediment-laden river floodwaters plunging into the sea
502 (Mulder et al., 2003). Catastrophic drainage events such as glacial outburst flood and dam-breaks
503 can also generate hyperpycnites (e.g., St-Onge et al., 2004; Mulder et al., 2009; Mulder and
504 Chapron, 2011; Duboc et al., 2017). To our knowledge, this is the first report of a hyperpycnal
505 deposit in a fabricated structure. How did a hyperpycnite form in Canale Traverso? Did the high-
506 intensity flow have natural causes, such as in association with a river flood, storm, or tsunami event,
507 or was it human-induced such as through opening of a canal gate, or from dredging? The hypothesis
508 of a major river flood is ruled out by the presence of a thick central debris layer in unit C. While a
509 typically steady and sustained flood flow carries a suspended load over hours to weeks, the debris
510 layer of unit C instead indicates bedload transport during a short-duration high-energy flow.
511 Tsunami or extreme storm waves are high-energy, short-duration events that form graded deposit

512 with debris (Robke and Vött, 2017). A single fining upward sequence (waning flow) is typically
513 reported for such events, but the coarsening upward sequence (waxing flow) observed in Canale
514 Traverso could have been generated by inflow and backflow events from the sea, travelling in the
515 harbour basins, and up the canals. However, there is no erosive contact at the base of unit C as may
516 be expected for a tsunami, the debris layer has a clear fluvial signature (Table 3), and previous
517 combined geophysical surveys, sedimentological, macro- and microfossil, and geochemical
518 analyses have not revealed a tsunamite in Portus (Delile et al., 2014; DiBella et al., 2011; Goiran et
519 al., 2010; Pepe et al., 2013; Sadori et al., 2010; Salomon et al., 2012; 2014).

520 Assuming that the deposit tracked the flow hydrograph, the presence of debris and an erosive
521 contact are key to identifying the type of flow and the conditions under which the hyperpycnite
522 formed (Mulder, 2003). According to Mulder (2003), the debris layer located below the fining
523 upward sequence and the absence of an erosive basal contact in unit C best correspond to a natural
524 dam-break event. Erosion of a natural sediment dam appears to be a good analogue for opening a
525 canal gate in a Roman harbour context. Opening Canale Traverso would have suddenly increased
526 water flow from the river (waxing flow; Fig. 8), eroding and transporting sediment and debris that
527 would have blocked the canal, or accumulated on the river side of the gate, and then water flow
528 would have decreased (waning flow; Fig. 8) until steady flow is reached. Another hypothesis is a
529 dredging-generated hyperpycnal deposit, where the fining upward sediment would be deposited by
530 suction under the dredging shovel. However, absence of an erosive contact between units B and C
531 does not support this idea, which also does not account for the coarsening-upward and debris layers
532 (Table 3). Based on multi-proxy sediment analysis and high-resolution stratigraphy, our preferred
533 interpretation for unit C is a canal dam-break hyperpycnal deposit (Fig. 8), which is an analogue for
534 natural dam-breaks in a fabricated structure.

535 4.3.3 Event deposits summary

536 Units B and C are consecutive event deposits. Our multi-proxy data set suggests that the event
537 deposits were human-induced, with our preferred interpretation of unit B being a dredged deposit,

538 and unit C being a canal dam-break hyperpycnal deposit (Table 3). The flood, tsunami or storm
539 hypotheses are plausible alternative interpretations for unit C, which was deposited under high-
540 energy hydrodynamic conditions. The hypothesised dredging event may have occurred during the
541 Trajanic redevelopment (AD 112-117) (Keay et al., 2005), based on age modelling and the presence
542 of different muds in the harbour deposit (unit D) and in the dredged deposit (mud clast sample 6-8).
543 Sediment mix and drop during dredging would have formed the dredged deposit, while waxing and
544 waning flows would have formed the hyperpycnal deposit (Fig. 8). For the first time, major event
545 deposits are described in Portus, and identification of a 159-cm-thick reworked sediment has
546 important implications for age-depth modelling and water depth reconstructions. The
547 Palaeoenvironmental Age-Depth Model (PADM) chart (Fig. 6A; Salomon et al., 2016) indicates
548 water depth based on core stratigraphy and reconstructed local relative sea level (Goiran et al.,
549 2009). The water depth in Canale Traverso after dredging (top of Unit C) was about 3 m, which
550 provides sufficient draught for ships 150 t and smaller, such as *Bourse de Marseille* and *Fiumicino*
551 *I* (Gassend, 1982; Pomey and Tchernia, 1978; Pomey and Rieth, 2005; Boetto, 2010).

552 4.4 Canal Gate Usage

553 Were canal gates used in Portus for flood control? Tiber floods in the early first century AD had
554 silted the fluvial harbour of Ostia, which was then abandoned (Goiran et al., 2014; Hadler et al.,
555 2015). It is probable that the Romans used canal gates for flood management in Portus considering
556 that a main motivation for canal construction was to free Rome from flood dangers (AD 46
557 inscription - Thylander, 1952: B310 = CIL XIV 85 = ILS 207; and AD 102-109 inscription -
558 Thylander 1952: B312 = CIL XIV 878 = CIL VI 964 = ILS 5797a; Keay et al., 2005). Canal gate
559 technology was presumably used as early as the 3rd century BC by Ptolemy II in the Ancient Suez
560 Canal, which was re-built by Trajan (Moore, 1950). The major redevelopment of Portus by Trajan
561 in AD 112-117 (Keay et al., 2005) took place soon after a catastrophic Tiber flood as reported by
562 Pliny the Younger in the winter of 108-109 AD (Syme, 1985). However, it is unknown if and how
563 that flood impacted Portus. We now evaluate if multi-proxy analysis of the harbour deposit in core
564 CPS1 (unit D) is consistent with canal gate use.

565 The hyperpycnal deposit has a clear fluvial input signature. Sub-unit D2 has a similar fluvial
566 signature, with peak values of EM1, HIRM, pyroxene, and higher smectite/(illite+chlorite) ratio
567 (Fig. 3). However, there are significant differences, including the absence of an erosive contact or
568 discontinuity in D2, no grading, unchanged magnetic particle concentrations (Fig. 2), and no
569 flattened paleomagnetic inclinations (Fig. 9A). These results indicate that D2 is not an event
570 deposit, but rather a harbour deposit with marked river input over a period of about 60 years. Grain
571 size, magnetic, and bulk mineralogical data clearly indicate increased sand content, increased
572 fluvial magnetic particle populations (EM1), and coarser detrital minerals in D2 relative to the
573 previous harbour deposit D1 (Fig. 3). The D90-D50 diagram also indicates greater hydrodynamic
574 energy for D2 relative to D1 (Fig. 5F). These results are consistent with ostracod and pollen
575 analyses, which indicate greater freshwater input in the upper part of the harbour sequence in core
576 S5 (location on Figure 1; Sadori et al., 2010), as well as increased magnetic susceptibility in core
577 TR14 (Figs. 1 and 7; Delile et al., 2014). Together, the results can be interpreted as: (1) sub-unit D2
578 being deposited in an open Canale Traverso configuration that connected the Tiber River and the
579 harbour basins after a gate-controlled period (sub-unit D1), and/or (2) rapid climate change to
580 wetter conditions and stronger fluvial impact in the early 3rd century AD. River input proxies for
581 sub-unit D1 (Fig. 3) do not have coeval peak values. Only the clay mineral indicator has peak
582 values such as in the hyperpycnal deposit and D2. It is possible that if the coarser grains tracked by
583 EM1, HIRM, and pyroxene content were blocked from Canale Traverso by canal gates, finer clay
584 particles may have flowed over the gates during flood events or reached the canal by local runoff in
585 Portus. Overall, reduced river input in D1, sulphidic diagenetic conditions indicated by increased
586 pyrite formation, and warmer and more saline conditions indicated by higher gypsum content (Fig.
587 3) are consistent with D1 being deposited under gate controlled conditions. The multi-proxy dataset
588 provides abundant evidence in support of the idea of canal gate usage for water flow management.
589 The period of sub-unit D2 corresponds to the onset of Roman Empire contraction which is
590 characterized by increased climate instability (Büntgen et al., 2011), political turmoil, cultural

591 change, socio-economic instability (Duncan-Jones, 2006), and human health issues such as the
592 large-scale Plague of Cyprian (AD 251-266; Vuorinen, 1997). Thus, climatic or socio-economic
593 instabilities could possibly explain a sudden change in harbour management and canal gate
594 operation, and the later decommissioning of Canale Traverso. The capacity to close the only inland
595 waterway from the Tiber River to the capital city's harbour basins would undoubtedly have been
596 advantageous during flood events and at times of war. The sedimentary archives in Portus have an
597 undeniably strong anthropogenic influence; the depositional basin itself is man-made and the site
598 has witnessed intense human activity. Core CPS1 provides evidence of over one and a half centuries
599 of nearly annually-resolved harbour occupation at the height of the Roman Empire, with humans
600 using technologies in response to natural environmental and societal stresses.

601 5. CONCLUSIONS

602 Multi-proxy and high-resolution sediment analysis, including piston coring, core scanning, grain
603 size, paleo- and rock-magnetism, bulk and clay mineralogy, and radiocarbon dating was applied in
604 an ancient harbour context to understand its history. This method revealed 159 cm of event deposits
605 (units B and C) and 249 cm of harbour sediment (Unit D) in core CPS1. Without piston coring, a
606 fine stratigraphy would not be preserved and it is likely that the suggested dredged deposit (Unit B)
607 would be indiscernable from the pre-harbour deposit (unit A), and most crucially for water depth
608 reconstruction, the 66-cm-thick hyperpycnal deposit (Unit C) would have been included in the
609 harbour deposit (Unit D). Portus core correlation was achieved using magnetic susceptibility and
610 age modelling, and a chronostratigraphic marker at the time Canale Traverso was decommissioned
611 is proposed to reconcile previous core interpretations. Piston coring, whole core CT-scanning, and
612 magnetic analyses have proven useful for event stratigraphy and geoarchaeology. Routine analysis
613 of the type presented here could greatly improve chronostratigraphic analysis and water depth
614 reconstruction of ancient harbour deposits.

615 Our works also provides rare insights into Roman harbour technologies. Dredging activity in Canale
616 Traverso during the Trajanic-Hadrianic period (2nd century AD) provides a well-supported

617 hypothesis for explaining unit B. The dredging event has not been reported previously and predates
618 the known 4th century AD dredging depicted in a Roman epigraph. Portus was built in a delta,
619 without bedrock that may hold direct evidence of canal gates. While future excavation of canal
620 walls may provide direct evidence, this work provides indirect sedimentological indicators
621 consistent with hypothesised canal gates at Portus, and supports the ideas of Testaguzza (1970) and
622 Salomon et al. (2014). Magnetic analysis has been applied here to ancient harbour geoarchaeology
623 for the first time. It has proven useful at Portus for core correlation (magnetic susceptibility),
624 identification of event deposit (paleomagnetic inclination, κ_{ARM}/κ , IRM acquisition), and for
625 providing a river input proxy (S-ratio, HIRM, IRM acquisition). Sedimentary magnetism is a
626 versatile tool that can, therefore, be added to the geoarchaeologist's toolkit (Marriner and
627 Morhange, 2007).

628 ACKNOWLEDGEMENTS

629 We thank Prof. Simon Key and the *Soprintendenza Speciale per il Colosseo, il MNR e l'Area*
630 *Archeologica di Roma, Sede di Ostia* for collaboration and access to the site; the drilling team of
631 Guillaume Lopez, Régis Batteux, and Éric Semin (CETE Marseille); and Jacques Labrie and
632 Alexandra Leclerc for laboratory work at ISMER and INRS-ETE. Thanks to the editors and
633 reviewers for invaluable and constructive reviews. This work was supported by a postdoctoral
634 fellowship of the *Fonds de recherche du Québec pour la nature et les technologies* (FRQNT) and
635 La Trobe University Transforming Human Societies RFA and DVCR Research Fellowships to A.
636 Lisé-Pronovost, and by the Natural Sciences and Engineering Research Council of Canada
637 (NSERC) Discovery grants to G. St-Onge and J.-C. Montero-Serrano. The Young Scientist
638 Program of the Agence Nationale de la Recherche (ANR 2011 JSH3 002 01) and the European
639 Research Council ("Roman Mediterranean Ports program" under the European Union's Seventh
640 Framework Programme – FP7/2007-2013 / ERC grant agreement n°339123) provided financial and
641 logistical support. Fieldwork was supported by a Geological Society of America (GSA) graduate
642 scholarship, and radiocarbon dating and particle grain size analysis were supported by a research

643 grant from the Australian Institute of Nuclear Science and Engineering (AINSE ALNGRA15016) to
644 A. Lisé-Pronovost. We also acknowledge the help of radiocarbon laboratory staff and financial
645 support for the Centre for Accelerator Science at ANSTO, where the measurements were done,
646 through the Australian National Collaborative Research Infrastructure Strategy (NCRIS).

647 REFERENCES

- 648 Allen, W., 1853. The Ancient Harbour of Seleucia, in Pieria. *Journal of the Royal Geographical*
649 *Society of London* 23, 157-163.
- 650 Barton, C. E., McElhinny, M. W., Edwards, D. J., 1980. Laboratory studies of depositional DRM,
651 *Geophysical Journal of the Royal Astronomical Society* 61, 355-377.
- 652 Bellotti, P., Calderoni, G., Rita, F.D., D'Orefice, M., D'Amico, C., Esu, D., Magri, D., Martinez,
653 M.P., Tortora, P., Valeri, P., 2011. The Tiber River delta plain (Central Italy): coastal evolution
654 and implications for the Ancient Ostia Roman settlement. *The Holocene* 21, 1105-1116.
- 655 Benito, G., Macklin, M. G., Zielhofer, C., Jones, A. F., Machado, M. J., 2015. Holocene flooding
656 and climate change in the Mediterranean. *Catena* 130, 13-33.
- 657 Blott, S.J. and Pye, K., 2001. GRADISTAT: a grain size distribution and statistics package for the
658 analysis of unconsolidated sediments. *Earth Surface Processes and Landforms* 26, 1237–1248.
- 659 Bockius, R., 2014. Künstliche Schiffahrtswege, Wasserbau und Hydrotechnische Einrichtungen im
660 Altertum. In: P. Ettel/F. Daim/S. Berg-Hobohm et al. (Ed.), *Großbaustelle 793. Das Kanalprojekt*
661 *Karls des Großen zwischen Rhein und Donau. Mosaiksteine. Forschungen am Römisch-*
662 *Germanischen Zentralmuseum* 11 (Mainz 2014) 87–94.
- 663 Boetto, G. “Le Port vu de La Mer: L’apport de L’archéologie Navale À L’étude Des Ports
664 Antiques.” *Bolletino Di Archeologia Online* Special issue: XVII International Congress of Classical
665 Archaeology, Roma 22-26 Septembre 2008 (2010): 112–28. Bout-Roumazeilles, V., Cortijo, E.,
666 Labeyrie, L., Debrabant, P., 1999. Clay mineral evidence of nepheloid layer contribution to the
667 Heinrich layers in the Northwest Atlantic. *Palaeogeography Palaeoclimatology Palaeoecology* 146,
668 211–228.
- 669 Bravard, J.-P., and Peiry, J. L., 1999. The CM pattern as a tool for the classification of alluvial
670 suites and floodplains along the river continuum. *Geological Society London Special*
671 *Publications* 163, 259–268.
- 672 Bronk Ramsey, C., and Lee, S., 2013. Recent and Planned Developments of the Program OxCal.
673 *Radiocarbon* 55 (2-3), 720-730.

- 674 Brown, G. and Brindley, G.W., 1980. X-ray diffraction procedures for clay mineral identification.
675 In: Brindley, G.W., Brown, G. (Eds.), *Crystal Structures of Clay Minerals and their X-ray*
676 *Identification*. Mineralogical Society, London, pp. 305–359.
- 677 Büntgen, U., Willy Tegel, W., Nicolussi, K., McCormick, M., Frank, D., Trouet, V., Kaplan, J. O.,
678 Herzig, F., Heussner, K.-U., Wanner, H. Luterbacher, J. Esper, J., 2011. 2500 Years of European
679 Climate Variability and Human Susceptibility, *Science* 331 (6017), 578-582.
- 680 Camuffo, D. and Enzi, S., 1995. The analysis of two Bi-millenary series: Tiber and Po river floods.
681 In: Jones, P.D., Bradley, R.S., Jouzel, J. (Eds.), *Climatic variations and forcing mechanisms of*
682 *the last 2000 years*. NATO ASI Series, Series I: Global Environmental Change. vol. 41. Springer
683 Verlag, Stuttgart, 433–450.
- 684 Coccia, F., 1993. Il “Portus Romae” fra tarda antichità ed altomedioevo. In L. Paroli and P. Delogu
685 (Eds.), *Storia economica di Roma nell’Altomedioevo alla luce dei recenti scavi archeologici*.
686 Firenze: Atti del Seminario di Roma, 183–188, “All’Insegna del Giglio.”
- 687 Dankers, P., 1981. Relationship between median destructive field and remanent co-ercive forces for
688 dispersed natural magnetite, titanomagnetite and hematite. *Geophysical Journal of the Royal*
689 *Astronomical Society* 64, 447–461.
- 690 Day, R., Fuller, M., Schmidt, V.A., 1977. Hysteresis properties of titano-magnetite: grain size and
691 compositional dependence. *Physics of the Earth and Planetary Interiors* 13, 260-267.
- 692 Delile, H., Mazzini, I., Blichert-Toft, J., Goiran, J.-P., Arnaud-Godet, F., Salomon, F., Albarède, F.,
693 2014. Geochemical investigation of a sediment core from the Trajan basin at Portus, the harbour
694 of ancient Rome. *Quaternary Science Reviews* 87, 34-45.
- 695 Dearing, J.A., 1999. *Environmental Magnetic Susceptibility: Using the Bartington MS2 System*.
696 Chi Pub., Kenilworth.
- 697 Duboc, Q., St-Onge, G., Lajeunesse, P. 2017. Sediment records of the influence of river damming
698 on the dynamics of the Nelson and Churchill Rivers, western Hudson Bay, Canada, during the
699 last centuries. *The Holocene* 27, 712-725.
- 700 Duncan-Jones, R. P., 2006. Economic change and the transition to Late Antiquity, In: *Approaching*
701 *Late Antiquity: The Transformation from Early to Late Empire*, Eds. S. Swain, M. Edwards,
702 Oxford Univ. Press, Oxford, pp. 20–52.
- 703 Dunlop, D.J., Özdemir, Ö., 1997. *Rock Magnetism: Fundamentals and Frontiers*. Cambridge
704 University Press, Cambridge, New York.
- 705 Duchesne, M. J, Long, B. F., Labrie, J., Simpkin, P. G., 2006. On the use of computerized
706 tomography scan analysis to determine the genesis of very high seismic reflection facies, *Journal*
707 *of Geophysical Research* 111, B10103.

- 708 Egli, R., 2004. Characterization of individual rock magnetic components by analysis of remanence
709 curves. 1. Unmixing natural sediments. *Studia Geophysica et Geodaetica* 48, 391-446.
- 710 Erol, O., and Pirazzoli, P.A., 1992. Seleucia Pieria: an ancient harbour submitted to two successive
711 uplifts. *International Journal of Nautical Archaeology* 21(4), 317-327.
- 712 Evans, M.E. and Heller, F., 2003. Environmental magnetism: principles and applications of
713 enviromagnetics. In: *International Geophysics Series*, vol. 86. Academic Press, 299 p.
- 714 Eyre, J. K., 1997. Frequency dependence of magnetic susceptibility for populations of single-
715 domain grains. *Geophysical Journal International* 129, 209-211.
- 716 Fink, D., Hotchkis, M., Hua, Q., Jacobsen, G., Smith, A. M., Zoppi, U., Child, D., Mifsud, C., van
717 der Gaast, H., Williams, A., Williams, M., 2004. The ANTARES AMS facility at ANSTO, NIM
718 B 223-224, 109-115.
- 719 Finkler, C., Baika, K., Rigakou, D., Metallinou, G., Fischer, P., Hadler, H., Emde, K., Vött, A.,
720 2017. Geoarchaeological investigations of a prominent quay wall in ancient Corcyra –
721 implications for harbour development, palaeoenvironmental changes and tectonic
722 geomorphology of Corfu island (Ionian Islands, Greece). *Quaternary International*. In press.
723 Available online 16 May 2017.
- 724 Folk, R. L. and Ward, W. C, 1957. Brazos River bar, a study in the significance of grain size
725 parameters. *Journal of Sedimentary Petrology* 27, 3.
- 726 Fortin, D., Francus, P., Gebhardt, C, Hahn, A., Kliem, P., Lisé-Pronovost, A., Roychowdhury, R.,
727 Labrie, J., St-Onge, G., 2013. Destructive and non-destructive density determination: method
728 comparison and evaluation from the Laguna Potrok Aike sedimentary record, *Quaternary*
729 *Science Reviews* 71, 147-153.
- 730 Galli, P. and Molin, D., 2014. Beyond the damage threshold: the historic earthquakes of Rome,
731 *Bulletin of Earthquake Engineering* 12, 1277-1306.
- 732 Games, K. P., 1977. The magnitude of the paleomagnetic field: a new, non-thermal, non-detrital
733 method using sun-dried bricks. *Geophysical Journal of the Royal Astronomical Society* 48, 315-
734 329.
- 735 Games, K. P., 1983. Magnetisation of adobe bricks, In: *Geomagnetism of baked clays and recent*
736 *sediments*, Eds. Creer, K. M., Tucholka, P., Barton, C. E., Elsevier, 324 p.
- 737 Gassend, J. M. *Le Navire Antique Du Lacydon*. Musée d'Histoire de Marseille, 1982.
- 738 Gilli, A., Anselmetti, F. S., Glur, L., Wirth, S. B., 2013. Lake sediments as archives of recurrence
739 rates and intensities of past flood events, In: *Dating Torrential Processes on Fans and Cones* vol.
740 47, series *Advances in Global Research*, Eds. Schnewly-Bollschweiler, M., Stoffel, M., Rudolf-
741 Miklau, F., Springer, 423 p.

- 742 Giraudi C., Tata C., Paroli L., 2009. Late Holocene evolution of Tiber river delta and
743 geoarchaeology of Claudius and Trajan Harbour, Rome. *Geoarchaeology* 24, 371-382.
- 744 Goiran, J.-P., Salomon, F., Mazzini, I., Bravard, J.-P., Pleuger, E., Vittori, C., Boetto, G.,
745 Christiansen, J., Arnaud, P., Pellegrino, A., Pepe, C., Sadori, L., 2014. Geoarchaeology confirms
746 location of the ancient harbour basin of Ostia (Italy). *Journal of Archaeological Science* 41, 389–
747 398.
- 748 Goiran, J.-P., Tronchère, H., Salomon, F., Carbonel, P., Djerbi, H., Ognard, C., 2010.
749 Palaeoenvironmental reconstruction of the ancient harbours of Rome: Claudius and Trajan's
750 marine harbours on the Tiber delta. *Quaternary International* 216(1–2), 3–13.
- 751 Goiran, J.-P., Tronchère, H., Collalelli, U., Salomon, F., Djerbi, H., 2009. Découverte d'un niveau
752 marin biologique sur les quais de Portus: le port antique de Rome. *Méditerranée* 112 (1), 59-67.
- 753 Goiran, J.-P. and Morhange, C., 2001, Geoarcheology of ancient mediterranean harbours, *Topoi* 11
754 (2), 647-669.
- 755 Hadler, H., Vött, A., Fischer, P., Ludwig, S., Heinzemann, M., Rohn, C., 2015. Temple-complex
756 post-dates tsunami deposits found in the ancient harbour basin of Ostia (Rome, Italy). *Journal of*
757 *Archaeological Science* 61: 78-89.
- 758 Herries, A.I.R., 2009. New approaches for integrating palaeomagnetic and mineral magnetic
759 methods to answer archaeological and geological questions on Stone Age sites. In A. Fairbairn,
760 S. O'Conner and B. Marwick (Eds), *New Directions in Archaeological Science*, pp.235–253.
761 *Terra Australis* 28. Canberra: The Australian National University Press.
- 762 Heslop, D. and Dillon, M., 2007. Unmixing magnetic remanence curves without a priori
763 knowledge, *Geophysical Journal International* 170 (2), 556-566.
- 764 Heslop, D., 2015. Numerical strategies for magnetic mineral unmixing. *Earth-Science Reviews* 150,
765 256-284.
- 766 Hounsfield, G.N., 1973. Computerized transverse axial scanning (tomography): I. description of
767 system. *British Journal of Radiology* 46 (552), 1016-1022.
- 768 Key S., Millett, M., Paroli, L., Strutt, K., 2005. *Portus: an archaeological survey of the Portus of*
769 *imperial Rome*. Archaeological Monographs of the British School at Rome, 15, London.
- 770 Key, S. and Paroli, L., 2011. *Portus and its hinterland: recent archaeological research*.
771 *Archaeological Monographs of the British School at Rome*, 18, London.
- 772 Keller, G. and Pardo, A., 2004. Age and paleoenvironment of the Cenomanian–Turonian global
773 stratotype section and point at Pueblo, Colorado. *Marine Micropaleontology* 51, 95-128.
- 774 King, J., and Channell J. E. T., 1991. Sedimentary magnetism, environmental magnetism, and
775 magnetostratigraphy, in U.S. National Report to the International Union of Geodesy and
776 Geophysics vol. 29, pp. 358–370, AGU, Washington, D. C.

- 777 Kondolf, G. M., Gao Y., Annandale, G.W., Morris, G.L., Jiang, E., Zhang, J., Cao, Y., Carling, P.,
778 Fu, K., Guo, Q., Hotchkiss, R., Peteuil, C., Sumi, T., Wang, H.-W., Wang, Z., Wei, Z., Wu, B.,
779 Wu, C., Yang, C.T., 2014. Sustainable sediment management in reservoirs and regulated rivers:
780 Experiences from five continents, *Earth's Future* 2, 256-280.
- 781 Lisé-Pronovost, A., St-Onge, G., Gogorza, C., Haberzettl, T., Preda, M., Kliem, P., Francus, P.
782 Zolitschka, B. and the PASADO science team, 2013. High-resolution paleomagnetic secular
783 variation and relative paleointensity since the Late Pleistocene in Southern South America.
784 *Quaternary Science Reviews* 71, 91-108.
- 785 Lie, S., Li, S., Shan, X., Gong, C., Yu, X., 2017. Classification, formation, and transport
786 mechanisms of mud clasts. *International Geology Review* 59 (12), 1609-1620.
- 787 Liu, Q., Roberts, A.P., Larrasoana, J.C., Banerjee, S.K., Guyodo, Y., Tauxe, L., Oldfield, F., 2012.
788 *Environmental magnetism: Principles and applications. Reviews of Geophysics* 50, RG4002
- 789 Lurcock, P. C. and Wilson, G. S., 2012. PuffinPlot: A versatile, user-friendly program for
790 paleomagnetic analysis, *Geochemistry, Geophysics, Geosystems*, 13, Q06Z45,
- 791 Maher, B.A., 1988. Magnetic properties of some synthetic sub-micron magnetites. *Geophysical*
792 *Journal Royal Astronomical Society* 94, 83-96.
- 793 Marriner N., and Morhange, C., 2006. Geoarchaeological evidence for dredging in Tyre's ancient
794 harbour, Levant. *Quaternary Research* 65, 64–171.
- 795 Marriner, N. and Morhange, C., 2007. Geoscience of ancient Mediterranean harbours, *Earth*
796 *Science Reviews* 80, 137-194.
- 797 Marriner, N., Morhange, C., Doumet-Serhal, C., 2006. Geoarchaeology of Sidon's ancient harbours,
798 Phoenicia. *Journal of Archaeological Science* 33, 1514–1535.
- 799 Marriner, N., Kaniewski, D., Morhange, C., Flaux, C., Giaime, M., Vacchi, M., Goff, J., 2017.
800 *Tsunamis in the Geological Record: Making Waves with a Cautionary Tale from the*
801 *Mediterranean. Science Advances* 3 (10).
- 802 McCann, A.M., 1979. The Harbour and Fishery Remains at Cosa, Italy. *Journal of Field*
803 *Archaeology* 6 (4), 391-411.
- 804 McCormick, M., Büntgen, U., Cane, M. A., Cook, E. R., Harper, K., Huybers, P., Litt, T., Manning,
805 S. W., Mayewski, P. A., More, A. F. M., Nicolussi, K., Tegel, W., 2012. Climate Change during
806 and after the Roman Empire: Reconstructing the Past from Scientific and Historical Evidence,
807 *Journal of Interdisciplinary History* 43 (2), 169-220.
- 808 Mensing, S.A., Tunno, I., Sagnotti, L., Florindo, F., Noble, P., Archer, C., Zimmerman, S., Pavon-
809 Carrasco, F.J, Cifani, G., Passigli, S., Piovesan, G., 2015. 2700 years of Mediterranean
810 environmental change in central Italy: a synthesis of sedimentary and cultural records to interpret
811 past impacts of climate on society. *Quaternary Science Reviews* 116, 72-94.

- 812 Millet, B., Tronchère, H., Goiran, J.-P., 2014. Hydrodynamic modeling of the roman harbour of
813 Portus in the Tiber delta: the impact of the north-eastern channel on current and sediment
814 dynamics. *Geoarchaeology* 29, 357-370.
- 815 Montero-Serrano, J.C., Bout-Roumazeilles, V., Tribovillard, N., Sionneau, T., Riboulleau, A., Bory,
816 A., Flower, B., 2009. Sedimentary evidence of deglacial megafloods in the northern Gulf of
817 Mexico (Pigmy Basin). *Quaternary Science Reviews* 28, 3333–3347.
- 818 Montero-Serrano, J.C., Foellmi, K.B., Adatte, T., Spangenberg, J.E., Tribovillard, N., Fantasia, A.,
819 Suan, G., 2015. Continental weathering and redox conditions during the early Toarcian Oceanic
820 Anoxic Event in the northwestern Tethys: Insight from the Posidonia Shale section in the Swiss
821 Jura Mountains. *Palaeogeography Palaeoclimatology Palaeoecology* 429, 83–99.
- 822 Moore, F.G., 1950. Three Canal Projects, Roman and Byzantine. *American Journal of Archaeology*
823 54(2), 97-111.
- 824 Morhange, C., and Marriner, N., 2010. Paleo-Hazards in the Coastal Mediterranean: A
825 Geoarchaeological Approach. In Martini, I.P, and Chesworth, W. (Eds.), *Landscapes and*
826 *Societies*, Springer, 478 p.
- 827 Morhange, C., Blanc, F., Schmitt-Mercury, S., Bourcier, M., Carbonel, P., Oberlin, C, Prone, A.,
828 Vivent, D., Hesnard, A., 2003. Stratigraphy of late Holocene deposits of the ancient harbour of
829 Marseille, southern France. *The Holocene* 13 (4), 593–604.
- 830 Mort, H.P., Adatte, T., Keller, G., Bartels, D., Föllmi, K.B., Steinmann, P., Berner, Z., Chellai,
831 E.H., 2008. Organic carbon deposition and phosphorus accumulation during oceanic anoxic
832 event 2 in Tarfaya, Morocco. *Cretaceous Research* 29, 1008-1023.
- 833 Mulder, T., Syvitski, J.P.M., Migeon, S., Faugères, J.-C., Savoye, B., 2003. Marine hyperpycnal
834 flows: initiation, behavior and related deposits. A review. *Marine Petroleum Geology* 20, 861–
835 882.
- 836 Mulder, T., Zaragosi, S., Jouanneau, J.-M., Bellaiche, G., Guérinaud, S., Querneau, J., 2009.
837 Deposits related to the failure of the Malpasset Dam in 1959, an analogue for hyperpycnal
838 deposit from jökulhlaups. *Marine Geology* 260, 81-89.
- 839 Mulder, T., and Chapron, E., 2011, Flood deposits in continental and marine environments:
840 Character and significance, In R. M. Slatt and C. Zavala, Eds., *Sediment transfer from shelf to*
841 *deep water—Revisiting the delivery system: AAPG Studies in Geology* 61, p. 1–30.
- 842 Paroli, L., 2005. The Basilica Portuense. In *Portus: An Archaeological Survey of the Port of*
843 *Imperial Rome*, edited by S. Keay, M. Millett, L. Paroli, and K. Strutt, 258–68. *Archaeological*
844 *Monographs of the British School at Rome* 15. London.
- 845 Passega, R., 1964. Grain size representation by CM patterns as a geological tool. *Journal of*
846 *Sedimentary Petrology* 34, 830–847.

- 847 Petschick, R., 2000. MacDiff 4.2 Manual. MacDiff [Online]. Available from World Wide
848 Web:[http://www.geologie.unifrankfurt.de/Staff/Homepages/Petschick/Classicsoftware.html#Ma](http://www.geologie.unifrankfurt.de/Staff/Homepages/Petschick/Classicsoftware.html#MacDiff)
849 [cDiff](http://www.geologie.unifrankfurt.de/Staff/Homepages/Petschick/Classicsoftware.html#MacDiff).
- 850 Pliny. Natural History, Volume III: Books 8-11. Translated by H. Rackham. Loeb Classical Library
851 353. Cambridge, MA: Harvard University Press, 1940
- 852 Pomey, P., 1995. Les épaves grecques et romaines de la place Jules Verne à Marseille. *Compte-*
853 *Rendus Académie Inscriptions et Belles Lettres*, avril-juin, 459–484.
- 854 Pomey, P., and E. Rieth. *L'archéologie Navale*. Collection “Archéologiques.” Paris: Editions
855 Errance, 2005.
- 856 Pomey, P., and A. Tchernia. “Le Tonnage Maximum Des Navires de Commerce Romains.”
857 *Archeonautica*, no. 2 (1978): 233–51.
- 858 Reimer P.J., Bard E., Bayliss A., Beck J.W., Blackwell P.G., Bronk Ramsey C., Buck C.E., Cheng
859 H., Edwards R.L., Friedrich M., Grootes P.M., Guilderson T.P., Haflidason H., Hajdas I., Hatté
860 C., Heaton T.J., Hogg A.G., Hughen K.A., Kaiser K.F., Kromer B., Manning S.W., Niu M.,
861 Reimer R.W., Richards D.A., Scott E.M., Southon J.R., Turney C.S.M., van der Plicht, 2013.
862 IntCal13 and MARINE13 radiocarbon age calibration curves 0-50000 years calBP, *Radiocarbon*
863 55(4).
- 864 Röbbke, B.R., Vött, A. (2017): The tsunami phenomenon. *Progress in Oceanography* 159: 296-322.
- 865 Roberts, A. P., 2015. Magnetic mineral diagenesis, *Earth Science Reviews* 151, 1-47.
- 866 Roberts, A. P., Pike, C.R., Verosub, K.L., 2000. First-order reversal curve diagrams: a new tool for
867 characterizing the magnetic properties of natural samples. *Journal of Geophysical Research* 105
868 (B12), 28461-28475.
- 869 Sadler, P.M., 1981. Sediment accumulation rates and the completeness of stratigraphic sections,
870 *The Journal of Geology* 89 (5), 569-584.
- 871 Sadori, L., Giardini, M., Giraudi, C., Mazzini, I., 2010. The plant landscape of the imperial harbour
872 of Rome. *Journal of Archaeological Science* 37, 3294–3305.
- 873 Salomon, F., Delile, H., Goiran, J.-P., Bravard, J.-P., Keay, S., 2012. The Canale Di Comunicazione
874 Traverso in Portus: the Roman sea harbour under river influence (Tiber Delta, Italy).
875 *Géomorphologie* 1, 75–90.
- 876 Salomon, F., Goiran, J.-P., Bravard, J.-P., Arnaud, P., Djerbi, H., Kay, S., Keay, S., 2014. A
877 harbour-canal at Portus: a geoarchaeological approach to the Canale Romano: Tiber delta, Italy.
878 *Water History* 6, 31-49.
- 879 Salomon, F., Keay, S., Carayon, N., Goiran, J.-P., 2016. The Development and Characteristics of
880 Ancient Harbours—Applying the PADM Chart to the Case Studies of Ostia and Portus. *PLOS*
881 *ONE* 11(9) 0162587.

- 882 St-Onge, G., Mulder, T., Piper, D.J.W., Hillaire-Marcel, C. and Stoner, J.S. 2004. Earthquake and
883 flood-induced turbidites in the Saguenay Fjord (Québec): a Holocene paleoseismicity record.
884 *Quaternary Science Reviews* 23, 283-294.
- 885 St-Onge, G., Mulder, T., Francus, P., Long., B. 2007. Continuous physical properties of cored
886 marine sediments. In : C. Hillaire-Marcel et A. de Vernal (Eds.), *Proxies in Late Cenozoic*
887 *Paleoceanography*, Elsevier, pp. 63-98.
- 888 Stober, J. C., and Thompson, R., 1979. An investigation into the source of magnetic minerals in
889 some Finnish lake sediments, *Earth and Planetary Science Letters* 45, 464–474.
- 890 Stock, F., Knipping, M., Pint, A. Pint, Ladstatter, S., Delile, H., Heiss, A.G., Laermanns, H.,
891 Mitchell, P.D., Ployer, R., Steskal, M., Thanheiser, U., Urz, R., Wennrich, V., Bruckner, H.,
892 2016. Human impact on Holocene sediment dynamics in the Eastern Mediterranean - the
893 example of the Roman harbour of Ephesus. *Earth Surface Processes and Landforms* 41, 980-996.
- 894 Storen, E. N., Dahl, S. O., Nesje, A., Paasche, O., 2010. Identifying the sedimentary imprint of
895 high-frequency Holocene river floods in lake sediments: development and application of a new
896 method. *Quaternary Science Reviews* 29, 3021-3033.
- 897 Stuiver, M., Reimer, P.J., Reimer, R.W., 2017, CALIB 7.1 [WWW program] at <http://calib.org>
- 898 Syme, R., 1985. The dating of Pliny's latest letters, *The Classical Quarterly (New Series)* 35 (1),
899 176-185.
- 900 Tauxe, L., 1993. Sedimentary records of relative paleointensity of the geomagnetic field: theory and
901 practice. *Reviews of Geophysics* 31 (3), 319-354.
- 902 Testaguzza, O., 1970. *Portus: illustrazione dei porti di Claudio e Traiano*. Julia Editrice, Rome.
- 903 Vött, A., Hadler, H., Willershäuser, T., Ntageretzis, K., Brückner, H., Warnecke, H., Grootes, P.M.,
904 Lang, F., Nelle, O., Sakellariou, D., 2014. Ancient harbours used as tsunami sediment traps – the
905 case study of Krane (Cefalonia Island, Greece). In: Ladstätter, S., Pirson, F., Schmidts, T.
906 (Hrsg.): *Häfen und Hafenstädte im östlichen Mittelmeerraum von der Antike bis in byzantinische*
907 *Zeit. Neue Entdeckungen und aktuelle Forschungsansätze. Harbors and harbor cities in the*
908 *eastern Mediterranean from Antiquity to the Byzantine Period: Recent discoveries and current*
909 *approaches. Byzas 19, Veröffentlichungen des Deutschen Archäologischen Instituts Istanbul,*
910 *Österreichisches Archäologisches Institut Sonderschriften 52, Vol. II, S. 743-771. Istanbul.*
- 911 Vuorinen, H.S., 1997. *Diseases in the ancient world, Hippokrates (Helsinki)*, 74-97.
- 912 Weeks, R., Laj, C., Endigoux, L., Fuller, M., Roberts, A., Manganne, R., Blanchard, E., Goree, W.,
913 1993. Improvements in long-core measurements techniques: applications in paleomagnetism and
914 paleoceanography. *Geophysical Journal International* 114, 651-662.

915 **FIGURE CAPTIONS**

916 Figure 1. A) Location of Portus near the Tiber River in Italy and B) position of the coring sites,
917 including the stationary piston cores CPS1 and CPS4, and previous rotary cores discussed in the
918 text. κ is magnetic susceptibility. C) Modern and D) ancient configuration of Portus (modified from
919 Goiran et al., 2010). E) Piston coring of core CPS1 in September 2011.

920 Figure 2. The stratigraphy of core CPS1 is primarily based on A) CT number, B) gamma-ray
921 attenuation, C) magnetic susceptibility, and D) mud content. Core CT-scan images and photographs
922 are on the left, with the sampling log (cubes and u-channels) and simplified stratigraphic log with
923 the types of deposit for units A to F. Square symbols are used for data measured on cube samples,
924 and simple line for u-channel samples. The dashed line indicates the D1/D2 transition within the
925 harbour deposit. E) Typical grain size distributions for each deposit type.

926 Figure 3. Bulk, clay, and magnetic mineralogy results. A simplified stratigraphic log with deposit
927 type is shown on the left. The dashed line indicates the D1/D2 transition within the harbour deposit.

928 Figure 4. Magnetic end-member (EM) analysis with three components representing distinct
929 magnetic particle populations in core CPS1 obtained by unmixing 50 isothermal remanent
930 magnetization (IRM) acquisition curves (Heslop and Dillon, 2007; Heslop, 2015). A) IRM end-
931 members and B) down-core variations of the relative proportions of EM1, 2, and 3. Magnetic
932 properties and multi-proxy investigations indicate that EM1 represents detrital minerals of fluvial
933 origin, EM2 represents biogenic minerals from the harbour, and EM3 represents lower coercivity
934 multi-domain (MD) particles.

935 Figure 5. Magnetic grain size indicators. A) Coercivity ratio H_{cr}/H_c , B) magnetization ratio M_r/M_s ,
936 C) median destructive field of the anhysteretic remanent magnetization MDF_{ARM} , and D)
937 frequency-dependent magnetic susceptibility $\chi_{FD\%}$, compared with bulk grain size indicators E) mud
938 content, and F) D90 vs D50 biplot (Passega, 1964) for core CPS1.

939 Figure 6. Radiocarbon-based chronology for core CPS1. Bayesian age modelling of A) full CPS1
940 core in a Palaeoenvironmental Age-Depth Model (PADM) chart (Salomon et al., 2016) and B) the
941 harbour deposit. Light grey distributions are calibrated ages and dark grey are modelled ages with a
942 simple sequence Bayesian model performed with the Charcoal Outlier Model using OxCal v4.2.3
943 (Bronk Ramsey and Lee, 2013). A simplified stratigraphic log and lithology for units A to F are
944 shown.

945 Figure 7. Comparison of Portus core stratigraphy and magnetic susceptibility data along a NNW-
946 SSE transect. The cores are aligned at the proposed chronostratigraphic marker at the time of
947 decommissioning Canale Traverso. Debris dammed Canale Traverso at the access channel entrance
948 (core CPS1; this study) and resulted in more marine conditions in the access channel (core TR14;
949 Delile et al., 2014) and more fluvial conditions upstream in Canale Traverso (core CT1; Salomon et
950 al., 2012). The top of core TR14 is at -0.19 m relative to current sea level, core CPS1 at +0.3 m, and
951 CT1 at +1.8 m. See core locations in Figure 1.

952 Figure 8. Core CPS1 reconstructed depositional history.

953 Figure 9. Typical demagnetization plots, orthogonal projection diagrams, and stereonet projections
954 for A-B) the harbour deposit, C) the hyperpycnal deposit, and D) the dredged deposit.
955 Demagnetization steps considered for the principal component analysis (PCA) calculation are
956 indicated and highlighted in red. Stable and well defined paleomagnetic directions were obtained
957 for (A, B) harbour mud samples and most reworked deposits, with inclination values (bold) near the
958 expected GAD field value of 60.8° (D). In contrast, flattened to reversed polarity inclinations are
959 obtained within the high-energy flow (C).

960 Figure 10. Magnetic parameters for identified reworked deposits in core CPS1. Magnetic
961 susceptibility (κ), saturation magnetization (M_s), hard isothermal remanent magnetization (HIRM),
962 paleomagnetic inclination, the magnetic grain size indicator κ_{ARM}/κ_{LF} , and concentration of
963 magnetic population EM1 are proxies for the hyperpycnal deposit, with peak values in the central
964 debris layer. Grain size data indicate a typical hyperpycnite sequence, coarsening upward from
965 predominantly fine silts to coarse sands during the waxing flow, and fining upward to fine sands
966 during the waning flow. The dredged deposit has relatively homogenous properties within the sand,
967 with distinct values associated with mud clasts. Note that inclination values near the geocentric
968 axial dipole (GAD) value are recorded in the muddy sands of the dredged deposit.

969 **SUPPLEMENTARY FIGURES**

970 Sup. Figure 1. Results of rock- and paleo-magnetic pilot studies.

971 Sup. Figure 2. First-order reversal curve (FORC) diagrams and hysteresis loops for samples from
972 sub-units D1 and D2 of core CPS1.

973 **TABLES**

974 Table 1. Laboratory analyses performed on core CPS1.

975 Table 2. Radiocarbon dating of core CPS1, calibration, and age modelling.

976 Table 3. Summary of data and hypotheses for the event deposits of core CPS1

ACCEPTED MANUSCRIPT

Table 1. Laboratory analyses performed on core CPS1.

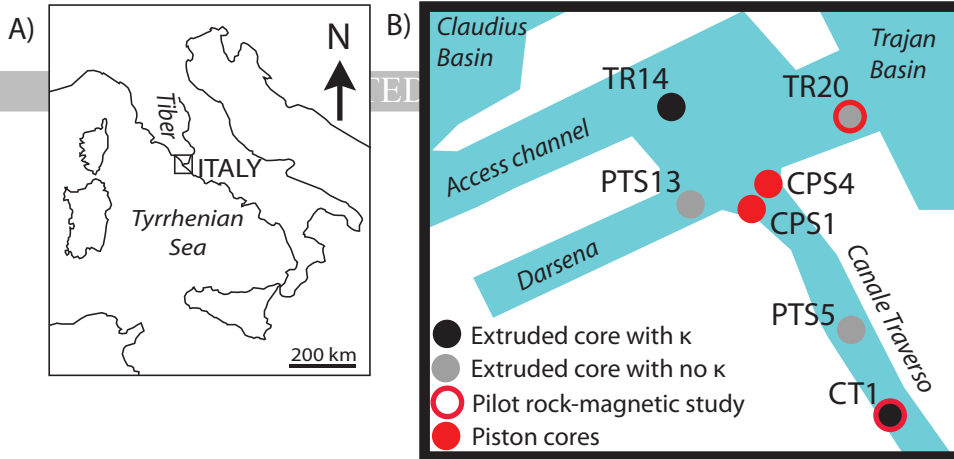
Analysis	Resolution
CT scan (density proxy)	0.06 cm
Gamma ray attenuation (density proxy)	1 cm
Volumetric magnetic susceptibility (κ)	1 cm
Image scan	0.025 cm
Volumetric magnetic susceptibility (κ)	0.5 cm
Natural remanent magnetisation (NRM)	1 cm
Anhysteretic remanent magnetisation (ARM)	1 cm
Frequency dependant magnetic susceptibility (χ_{FD})	10 cm
Laser granulometry (bulk grain size)	10 cm
X-ray diffraction (bulk mineralogy)	10 cm
Hysteresis curves and properties (M_r , M_s , H_{cr} , H_c)	10 cm
Isothermal remanent magnetisation (IRM) acquisition	10 cm
First-order reversal curves (FORC)	7 samples

Table 1. Radiocarbon dating of core CPS1, calibration, and age modelling.

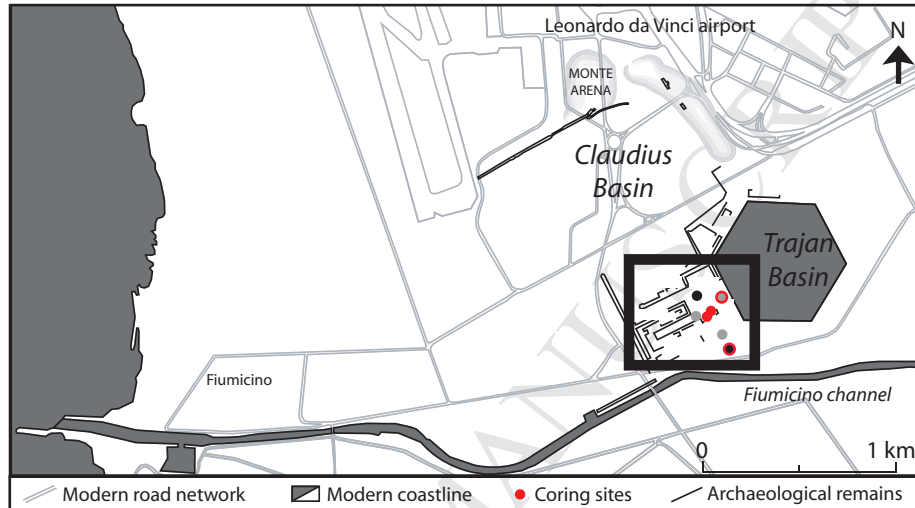
Core depth (cm)	Unit	Sample name	Laboratory code	Material	$\delta^{13}C$	^{14}C age (yr BP)	Calibrated age (AD/BC)		Modelled age (AD/BC)		
							min	max	min	max	median
170-171	D	CPS1-3/25-26cm	OZS602	pollen/charcoal	-25.0 ± 0.1	192 5 \pm 20	A D 28	AD 127	AD 16 3	AD 616	AD 294
227-228	D	CPS1-3/82-83cm	OZS601	coniferous bud	-24.5 ± 0.1	181 0 \pm 25	A D 13 1	AD 311	AD 15 5	AD 311	AD 220
269-270	D	CPS1-4/25-26cm	OZS600	seed	-23.8 ± 0.1	186 5 \pm 25	A D 80	AD 225	AD 14 0	AD 226	AD 186
357-358	D	CPS1-5/15-16cm	OZS599	seed	-25.3 ± 0.1	181 0 \pm 20	A D 13 1	AD 310	AD 12 8	AD 202	AD 155
414-415	C	CPS1-5/72-73cm	OZS598	pollen/charcoal	-25.0 ± 0.1	265 0 \pm 20	83 3 B C	795 BC	73 5 BC	AD 55	432 BC
580-581	A	CPS1-7/46-47cm	OZS597	seed	-26.2 ± 0.1	247 0 \pm 25	76 5 B C	492 BC	76 4 BC	434 BC	625 BC

Table 3. Summary of data and hypotheses for the event deposits of core CPS1.

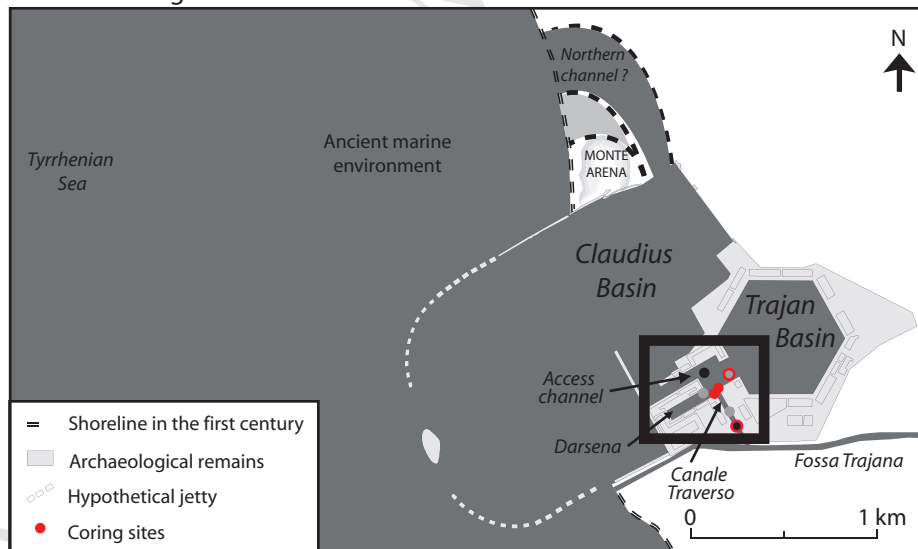
		Climate-driven		Human-driven	
		Tsunami	Flood	Canal gate	Dredging
		HIGH ENERGY FLOW			LOW ENERGY FLOW
Unit C	Fining upward				
	Debris layer (30 cm)				
	Fluvial signature of debris layer				
	Coarsening upward				
Unit B	GAD paleomagnetic inclination				
	Angular mud clasts				
	Massive (ungraded) sands				
	Erosive contact				

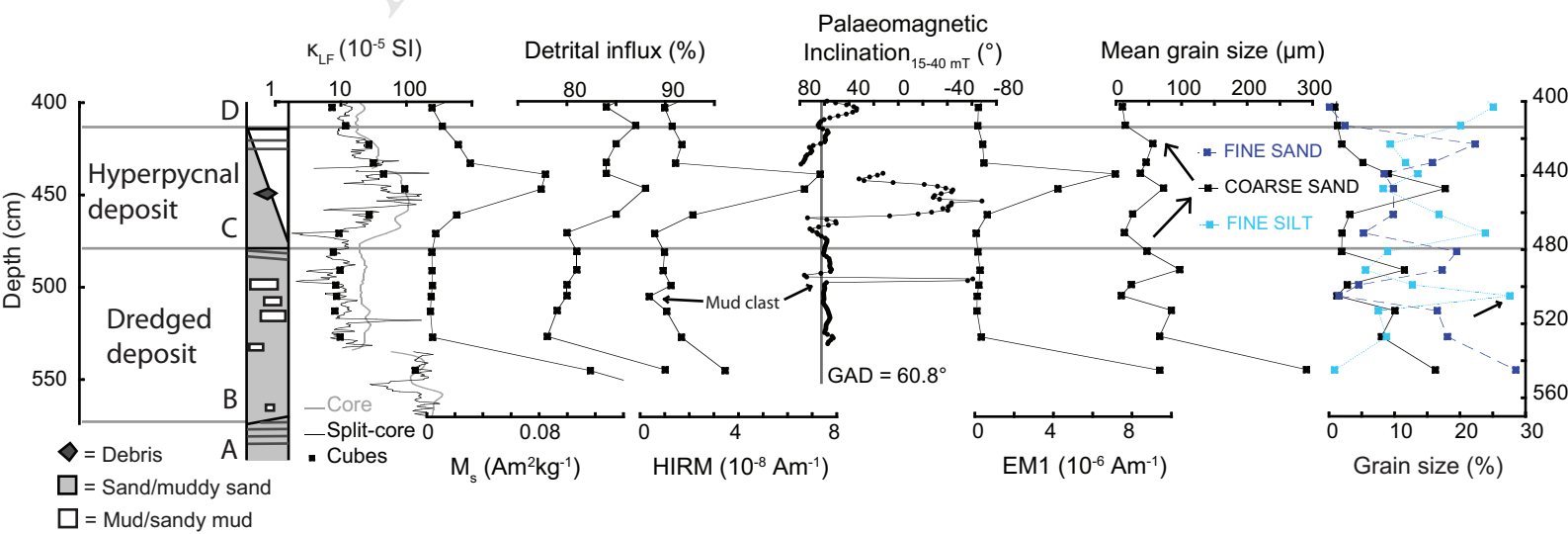


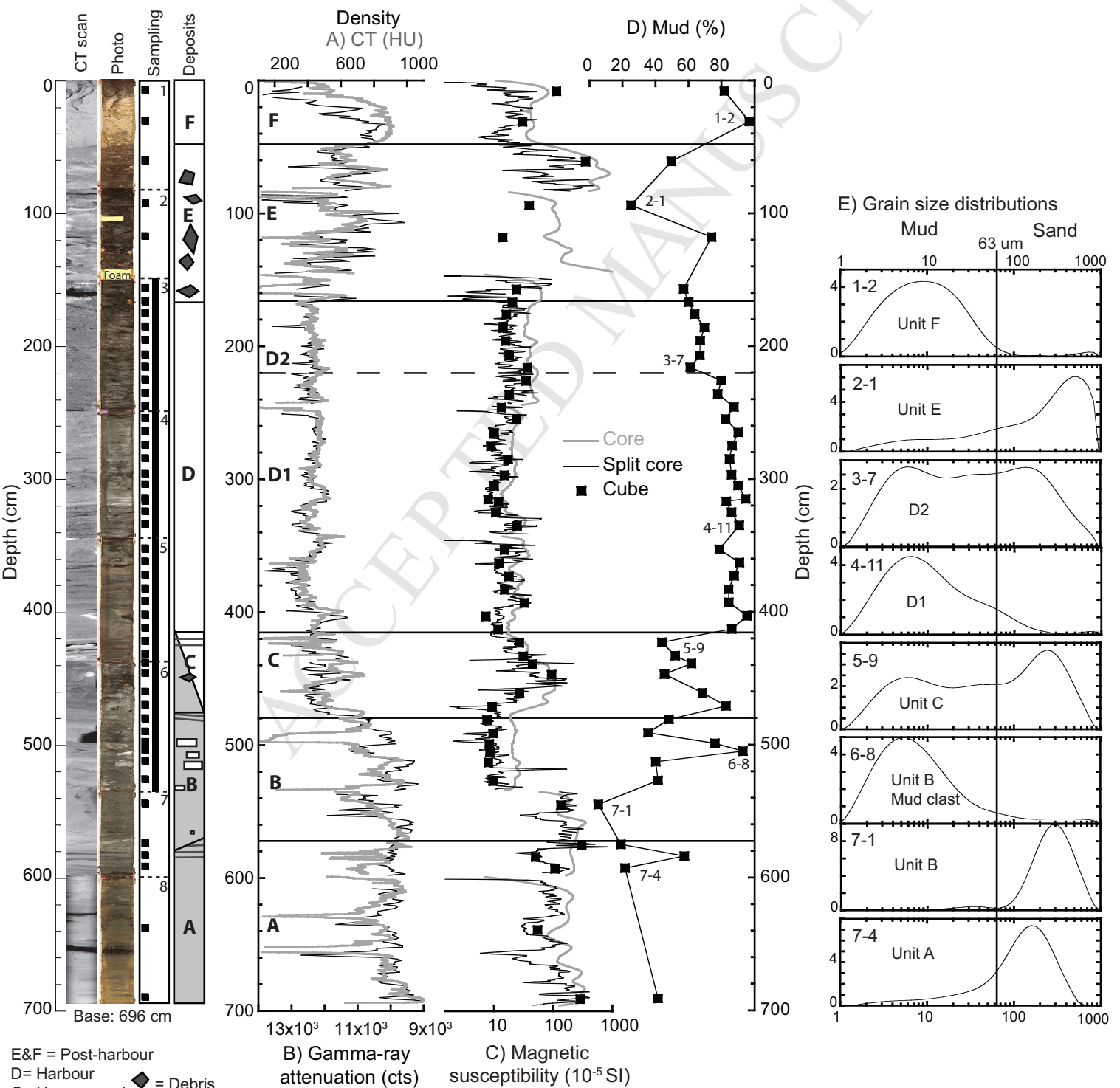
C) Modern configuration of the Portus area

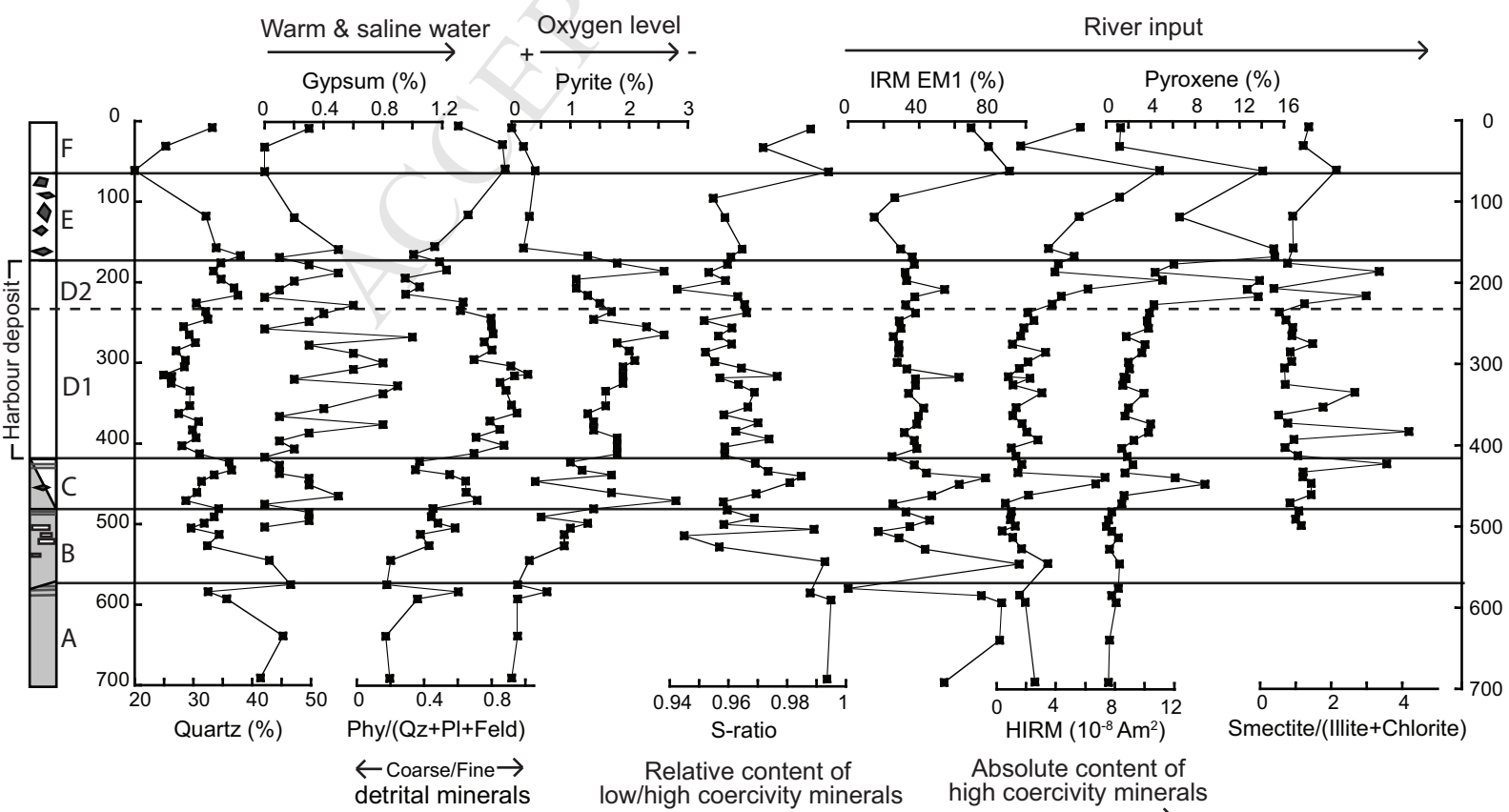


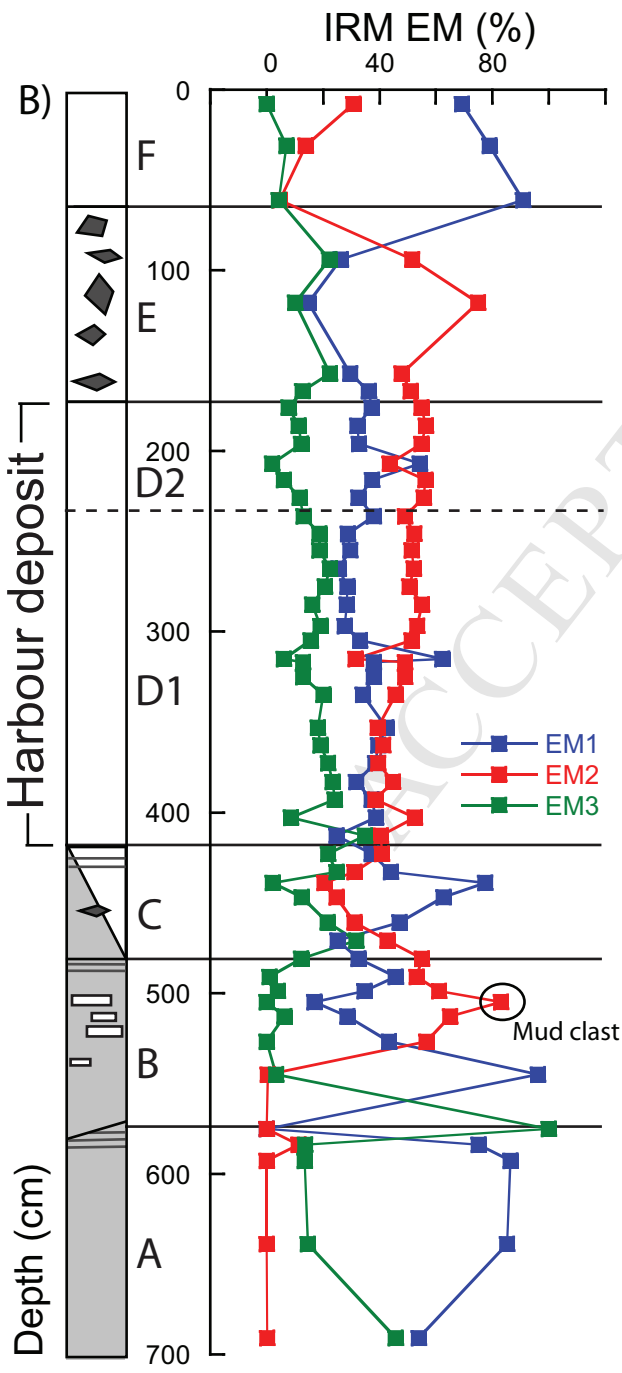
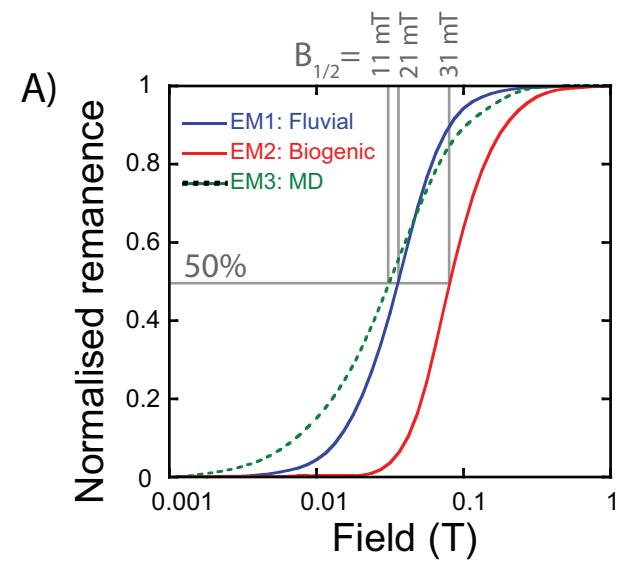
D) Ancient configuration of Portus

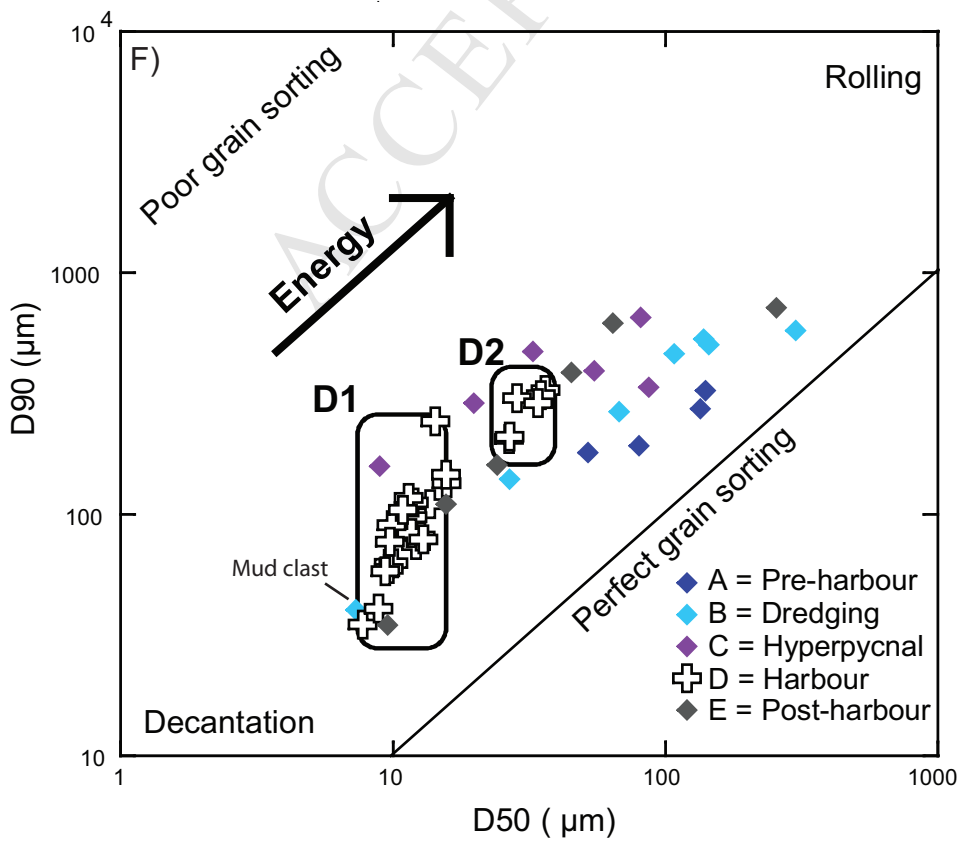
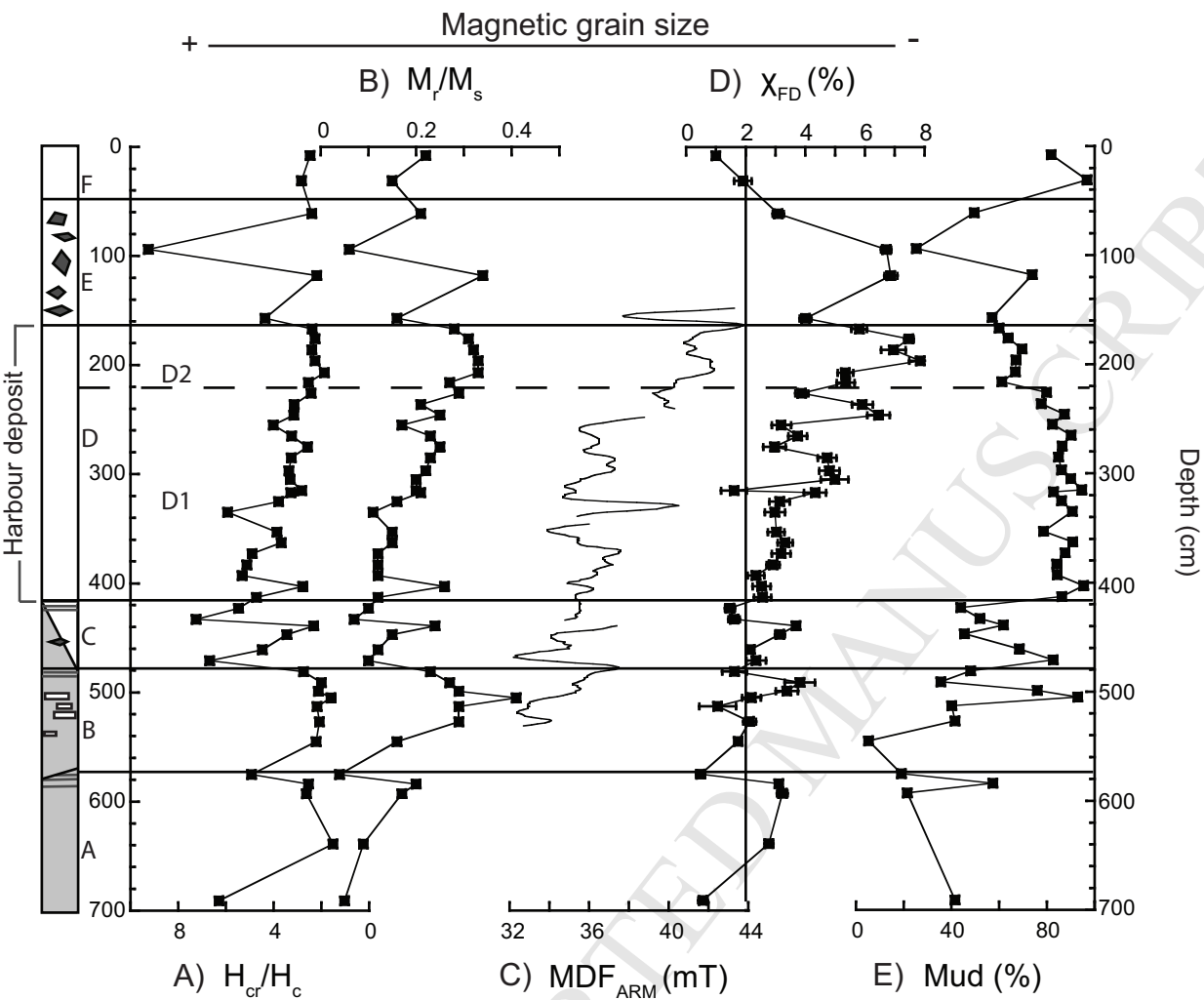




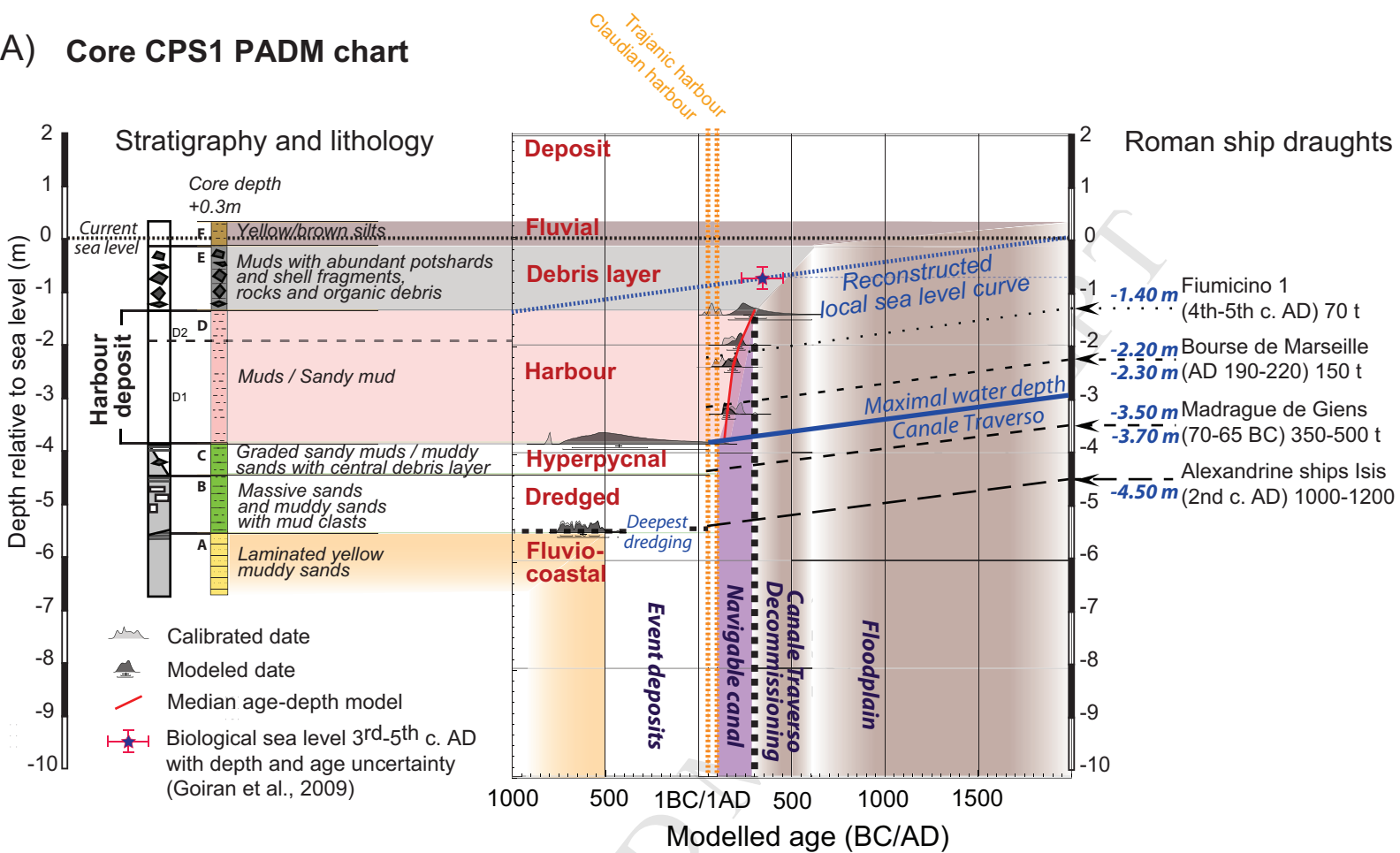




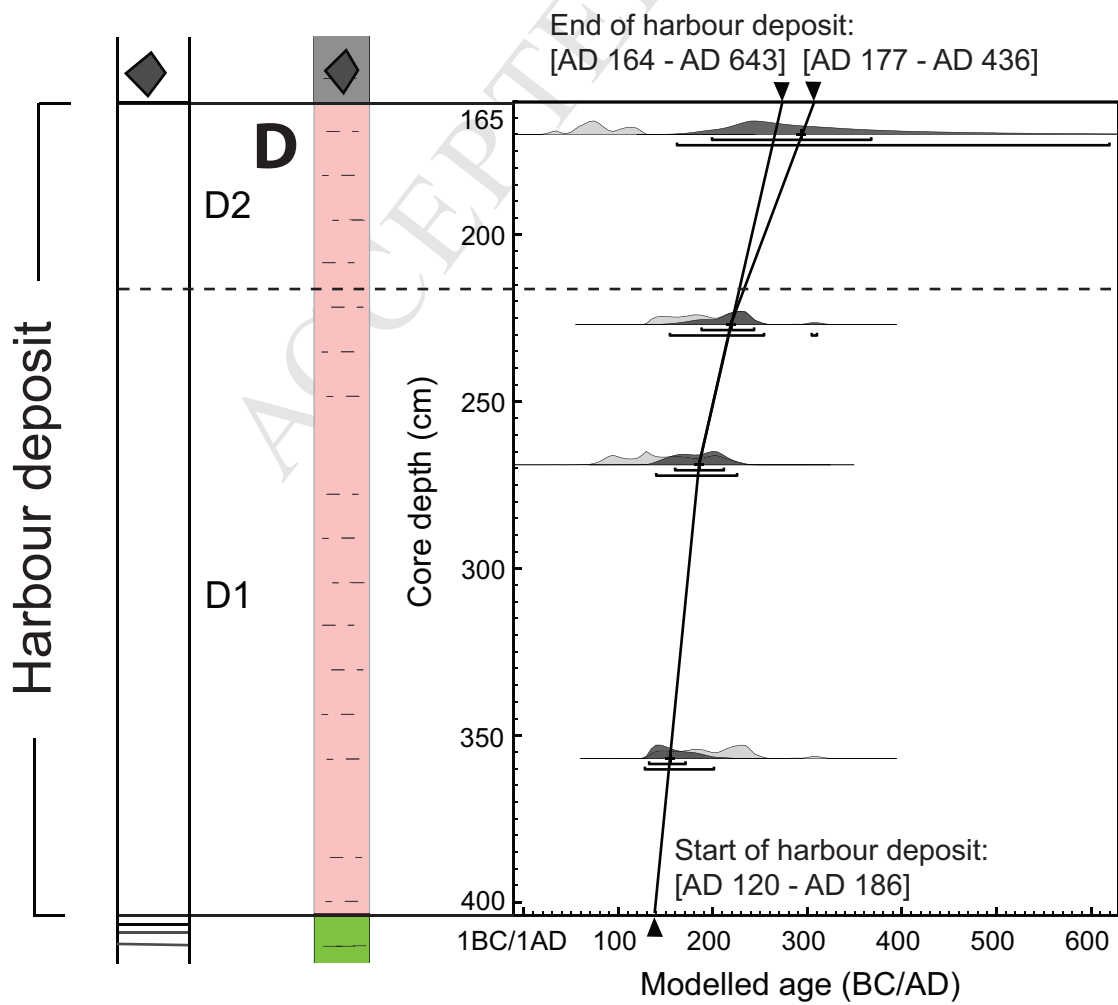


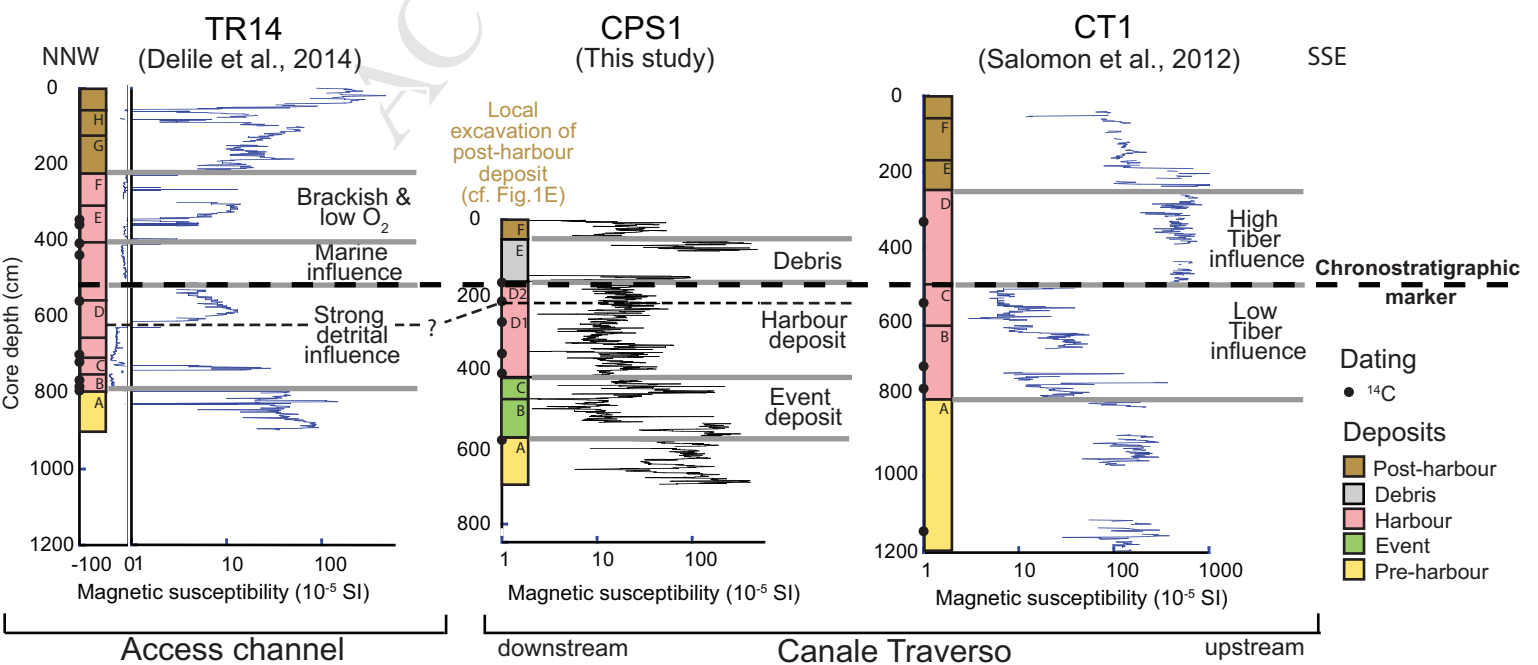


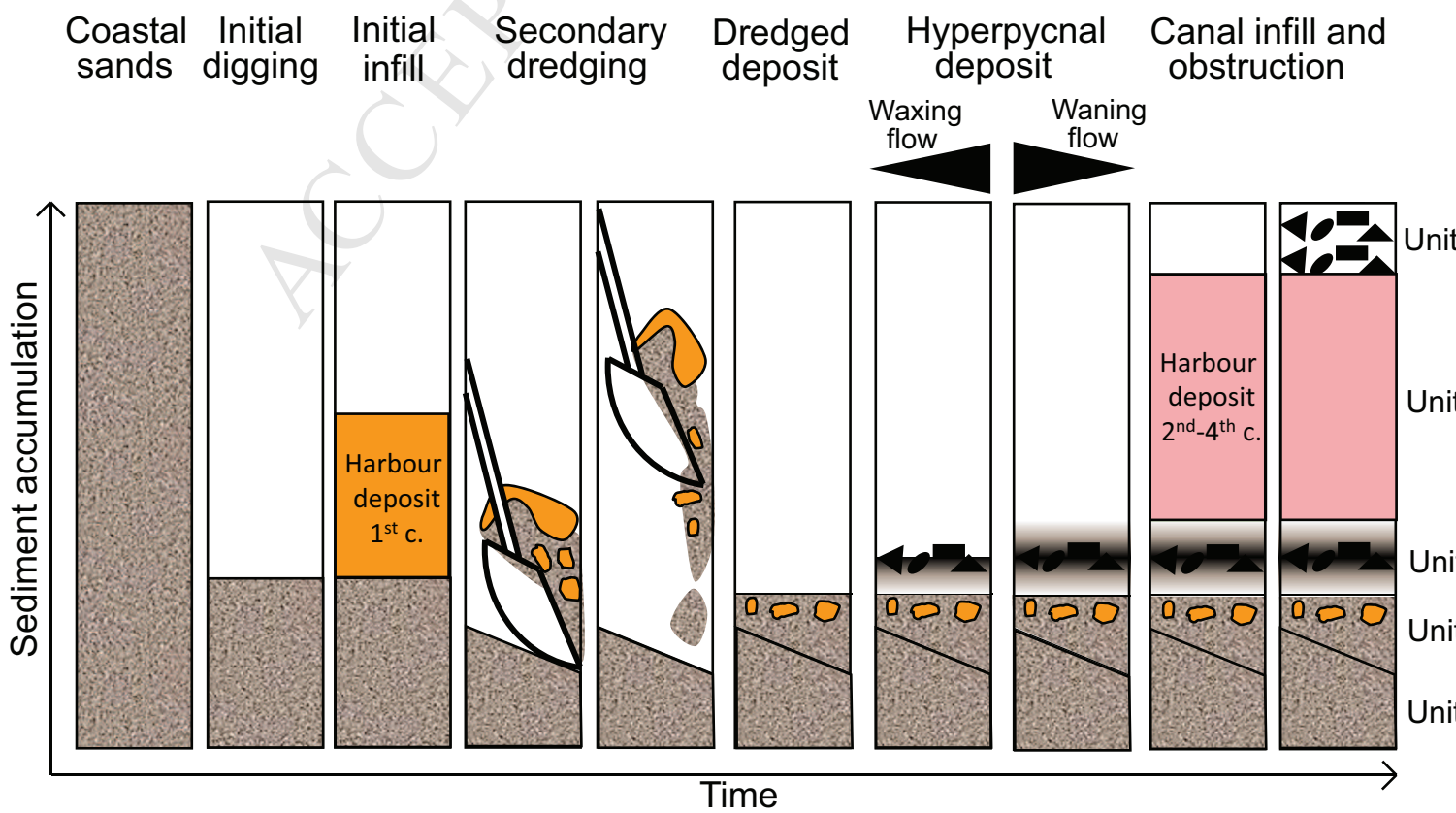
A) Core CPS1 PADM chart



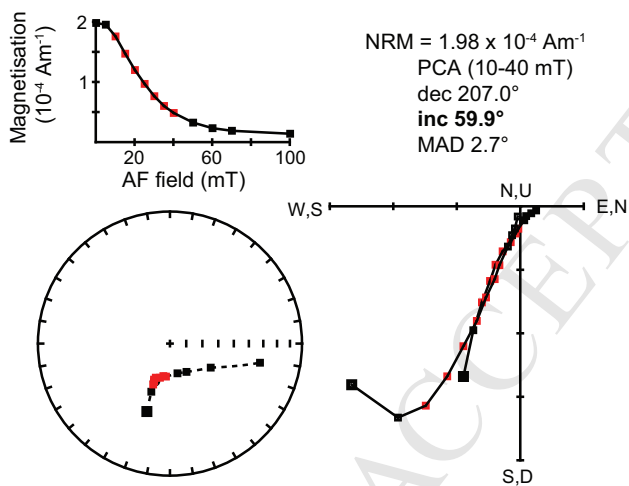
B)



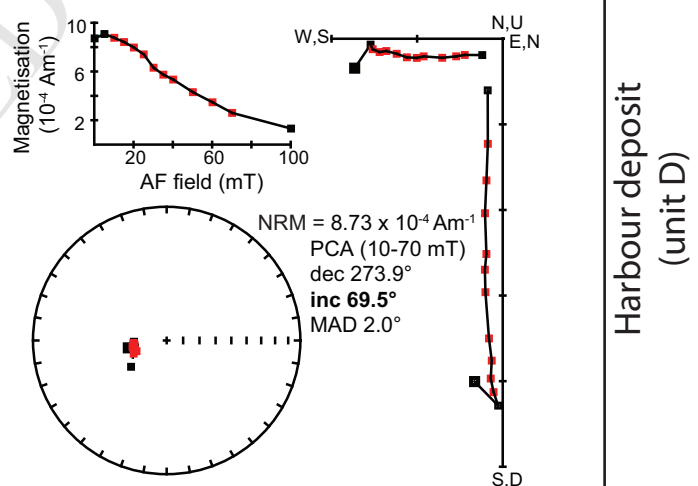




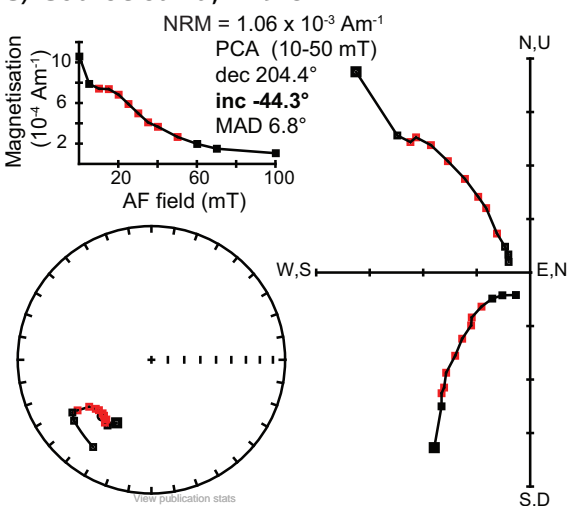
A) Mud sub-unit D2, 190 cm



B) Mud sub-unit D1, 327 cm



C) Coarse sand, 449 cm



D) Sand, 492 cm

